

Studies on the structure, optical, ac conduction mechanism by OLPT model and impedance spectroscopy of La-doped Ba₂SnO₄ Ruddlesden Popper Oxide

Upendra Kumar (✉ upendra.bhu512@gmail.com)

Indian Institute of Information Technology Allahabad <https://orcid.org/0000-0001-9200-0048>

Ram Sundar Maurya

Banasthali Vidyapith: Banasthali University

Harshpreet Cheema

Banasthali Vidyapith: Banasthali University

Vedika Yadav

Banasthali Vidyapith: Banasthali University

Aditya Kumar

University of Allahabad

P. A. Alvi

Banasthali Vidyapith: Banasthali University

Research Article

Keywords: La-doped Ba₂SnO₄, Rietveld Refinement, Raman spectroscopy; OLPT model, Impedance Spectroscopy.

Posted Date: June 24th, 2021

DOI: <https://doi.org/10.21203/rs.3.rs-646048/v1>

License:   This work is licensed under a Creative Commons Attribution 4.0 International License.

[Read Full License](#)

Studies on the structure, optical, ac conduction mechanism by OLPT model and impedance spectroscopy of La-doped Ba₂SnO₄ Ruddlesden Popper Oxide

Upendra Kumar^{1*}, Ram Sundar Maurya², Harshpreet Cheema², Vedika Yadav², Aditya Kumar³, P. A. Alvi²

¹Department of Applied Science, Indian Institute of Information Technology Allahabad, Jhalwa, Prayagraj-211015, Uttar Pradesh, India

²Department of Physics, Banasthali Vidyapith, Banasthali-304022, Rajasthan, India

³Center of Material Sciences, University of Allahabad, Prayagraj-211002, India

Abstract

The conventional ceramic route has been used to prepare the La-doped Ba₂SnO₄ samples by heat-treatment at 1000°C and sintered at 1250°C. The phase identification was carried out using XRD and found to be single phase up to 4 atoms %. The solubility of La at Ba-site were further reconfirmed using FTIR and Raman analysis. The AC conductivity spectra of all samples follow universal Johnscher's power law $\sigma_{ac} = \sigma_{dc} \left(1 + \left(\frac{f}{f_h}\right)^n\right)$; however, the thermal dependence of σ_{ac} and f_h suggest Arrhenius type conduction within the sample. Further, the scaled conductivity σ_{ac}/σ_{dc} and frequency f/f_h at all temperatures superimposes on a single master curve, indicates the invariance of conduction mechanism. The impedance spectroscopy studies suggest the major contribution of grain in the conduction and relaxation. The present material could be potentially used in semiconductor device, UV-detector, and mixed ionic and electronic conductor (MIECs) by utilizing absorption states and thermo-curves as metastable state.

Keywords: La-doped Ba₂SnO₄, Rietveld Refinement, Raman spectroscopy; OLPT model, Impedance Spectroscopy.

*Corresponding Author

Upendra Kumar (upendra.bhu512@gmail.com)

1. Introduction:

The ternary oxides belonging to the Ruddlesden Popper (RP) phase were identified by the general chemical formula $A_{n+1}B_nO_{3n+1}$, consisting of n-layered perovskite (ABO_3) slabs sandwiched along the c-axis by two rock salt layers of A-O [1–3]. Because of their exceptional electronic and ionic transmission behaviour, this form structure gained considerable interest from researchers in discovering its potential used in superconductors, supercapacitors, as thermoelectric materials, as multiferroic materials and as cathode materials for solid oxide fuel cells [4–9]. Due to their lower thermal expansion coefficients (TECs) than the conventional perovskite-based manganite, the rare earth-based nickelate, cobaltite, and ferrite were more extensively studied among the investigated K_2NiF_4 type phase [10–12]. Another advantage of these structures over perovskites is that perovskites have a compact structure, so they only have an oxygen deficiency phase, while RP phases have both an oxygen deficiency and an efficient phase. Because of this exceptional property, these typical structures can be used in mixed ionic and electronic conductor (MIEC) applications [1,13,14].

Rare-earth based nickelate/cobaltite Ln_2NiO_4/Ln_2CoO_4 (Ln: La, Pr, Nd) have been recognized as auspicious cathode materials due to their ability to replace conventional electrode materials used at high temperatures [7,10,11]. There are two types of oxygen sites in the structure: an equatorial oxygen site inside the perovskite, and an axial oxygen site that serves as a connection between the perovskite and the rock-salt layer [15]. The interstitial incorporation of oxygen between the perovskite and rock salt layers causes an extraordinarily large change in oxygen non-stoichiometry (δ) for solid oxide fuel cells at intermediate temperatures (IT-SOFCs). The transition metal was used as a source of conduction in these materials, which was accomplished through an oxidation (Ni^{2+}/Co^{2+} to Ni^{3+}/Co^{3+}) and reduction (Ni^{3+}/Co^{3+} to Ni^{2+}/Co^{2+}) process. A.P. Khandelwal et al. studied the electrical properties of Nd_2NiO_4 and reported that the replacement of alkali earth metals at the Nd-site improved mixed electronic and ionic conductivity [16]. By tuning the valence states of Fe, Chao Jin et al. mentioned that Sr substitution at the Ba-site of Ba_2FeO_4 could be used as a new cathode material for IT-SOFCs [17]. Since the chemical used in nickelates is so expensive, it's unlikely that these conventional materials will ever be commercialized in bulk. It is therefore essential to find an alternative to this material, not just for the development of new materials but also for the understanding of the fundamental solid-state physics. It has been noted on the basis of literature that alkaline earth-based stannates (M_2SnO_4 , M: Ca, Sr, Ba) completely fulfil the requisite requirements

possessed by La_2NiO_4 , La_2CoO_4 , Ba_2FeO_4 , etc. such as, (i) it has multivalent ion Sn, that exist in $\text{Sn}^{4+}/\text{Sn}^{2+}$, (ii) larger the volume for tuning the oxygen non-stoichiometry (δ).

Alkaline earth based stannates (M_2SnO_4) also belongs to the RP phase, which belongs to the space group $I4/mmm$ and crystallized into tetragonal structure ($a = b \neq c, \alpha = \beta = \gamma = 90^\circ$) [18]. Alkaline earth orthostannates have recently received more attention as a new phosphor material, owing to their stable crystalline nature and high physical and chemical stability [19]. Rare earth metals and transition metals were used to control the photoluminescence properties of the host phosphor material that are used in flat panel displays, field emission displays, and electroluminescence devices [20,21]. Detailed electrical properties of Ba_2SnO_4 have already been described in the literature; two types of conduction mechanisms have been found to be operative within the investigated temperature range, assigned to electronic conduction at low temperatures and ionic conduction at higher temperatures [15]. The modification in Ba_2SnO_4 lattice manipulates the sources of charge carriers and semiconducting properties that played the crucial role in the electrical properties. The doping of various atoms in the solids can be done on the basis of Hume-Rothery criteria [22]; the difference of ionic radii between the host and dopants should be lie below $\pm 15\%$. Since the difference between the ionic radii of La and Ba was found to be less than 15 %, this means that La is a suitable dopant for the Ba site of Ba_2SnO_4 . Since Ba_2SnO_4 consists of a perovskite BaSnO_3 and rock salt layer BaO , so it will be expecting that it might be show a cumulative property of BaSnO_3 and BaO . There are several reports available in literature on La-doped BaSnO_3 system [23–30]. Among the investigated papers, following are the investigations; K. K. James et al. prepared the thin film of La-doped BaSnO_3 at fused silica substrate using laser ablation, and found a progressive increase in conductivity up to 9 Scm^{-1} with incorporation of 7 at % La at Ba-site[27]. Q. Liu et al. also prepared the same thin film of La-doped BaSnO_3 using laser ablation and found a compositional dependence metal to semiconductor transition below room temperature[28]. Upadhyay et al. synthesized the nanopowder of La-doped BaSnO_3 system and studied their electrical properties using impedance spectroscopy and found their application as oxygen ion and hydroxyl ion conductor [29]. Masahiro et al. synthesized the ceramics of La-doped BaSnO_3 using polymerized complex method and reported it as n-type degenerate semiconductor [23]. The multifunctional application of La-doped BaSnO_3 enforce us to choose La as dopant for present system and will be expect to be as interesting as reported in literature. It is very interesting that no research has been available in the literature

so far on the partial substitution of La at the Ba site in Ba_2SnO_4 . Therefore, an attempt has been made in this manuscript to replace Ba with La in Ba_2SnO_4 .

In present investigation the synthesis of La doped at the site of Ba_2SnO_4 have been carried out using traditional ceramic route by calcining at 1000°C . The phase identification of the synthesized samples is confirmed using X-ray diffraction (XRD) followed by Rietveld refinement. The solubility limit of La in Ba_2SnO_4 lattice has been investigated by Raman spectroscopy and Fourier transform infrared spectroscopy (FTIR). The morphological and electrical properties of sintered ceramics were further studied using a field emission scanning electron microscope and a high precision LCR meter respectively.

2. Experimental:

The different compositions of $\text{Ba}_{2-x}\text{La}_x\text{SnO}_4$ (where $x = 0, 0.01, 0.02, 0.04, 0.06, 0.10$) have been prepared via traditional ceramic route using BaCO_3 , SnO_2 , and La_2O_3 as raw materials. The composition with different doping concentration was referred by abbreviated names; B2LS0 for $x=0$ and B2LS1 for $x=0.01$ and so on. For example, B2LS2 refers to the composition $\text{Ba}_{1.98}\text{La}_{0.02}\text{SnO}_4$. The raw materials have been weighed in stoichiometric ratio and mixed using acetone as mixing media with constant speed of rotation 200 rpm for 8 h in a ball – miller (Retsch PM-200). These prepared mixtures have been dried into an oven for 4 h, then transferred to an alumina crucible and heated at 1000°C for 6 h in ambient atmosphere. Temperature of the muffle furnace was increased at a constant heating rate of $5^\circ\text{C}/\text{min}$. The obtained mixture powder was evenly mixed with 2% polyvinyl alcohol (PVA) and pressed into cylindrical pellets with a diameter of 12 mm and a thickness of ≈ 2 mm using a uniaxial hydraulic press. The pellets have been air sintered into a muffle furnace; initially the temperature was increased to 200°C with constant heating rate of $2^\circ\text{C}/\text{min}$ and hold for 1 h to complete burn off the binder. Then, the temperature of furnace increased to 1250°C with constant heating rate of $5^\circ\text{C}/\text{min}$ and hold for 6 h. Thereafter, the furnace was normally cooled to room temperature. The sintered pellets were coated by conducting silver paste and firing at 400°C for 35 min to make perfect connection. Further, the silver coated pellets were projected for electrical properties measurement.

3. Characterization techniques:

The thermal analysis of prepared mixture was performed using thermogravimetric and differential scanning calorimetry (TGA/DSC) (Mettler Toledo) system from temperature 25- 1000°C at a constant heating rate of $10^\circ\text{C}/\text{min}$ in the presence of nitrogen gas. Crystal structure

and phase analysis of prepared samples were studied using Rigaku Miniflex II desktop, X-ray diffractometer (XRD) using Cu-K α radiation as source obtained at 30 kV and 20 mA and Ni as filter. The XRD patterns were collected within angular range of $20 \leq 2\theta \leq 80$ at a constant step size $\Delta 2\theta = 0.02^\circ$. The Fourier transform infrared (FTIR) spectra of obtained samples were recorded by Fourier Transform Infrared Spectrometer (Shimadzu, Model DF 803) using KBr pellet method within the wave number range of 400–4000 cm^{-1} . Raman spectra of prepared samples were recorded at room temperature using Raman spectrometer (Renishaw) equipped with a laser diode having wavelength 532 nm. To record the Raman spectra, the sample was focused by incident laser beam at a 50 \times long distance objective attached to the Leica DM 2500 M microscope. The optical properties of prepared samples were studied using UV-visible spectrophotometer (UV-2600, Shimadzu) from wavelength 200 to 800 nm in the absorption mode. The scanning electron micrograph (SEM) of the fractured surface of sintered pellets were recorded by a scanning electron microscope (JEOL JSM 840 A). Further, the electrical properties of sintered ceramics were measured using high precision LCR meter (Agilent E-4980A) in a wide range of temperature (300–600 $^\circ\text{C}$) and frequency (20 Hz–2 MHz).

4. Results and Discussion

4.1. Determination of calcination temperature

The thermogravimetric (TG) and differential scanning calorimetry (DSC) analyses of B2LS0 and B2LS2 were carried out to determine the calcination temperature for the prepared mixture of samples, as shown in Fig. 1 (a) and (b), respectively. The TG curve of B2LS0 shows weight loss of 9 % in a single step (700 $^\circ\text{C}$ -1000 $^\circ\text{C}$) whereas, B2LS2 shows weight loss of 17.08 % in two steps; first of 6.37 % 25 $^\circ\text{C}$ to 100 $^\circ\text{C}$ and the second of 10.71 % from 100 $^\circ\text{C}$ to 1000 $^\circ\text{C}$. Due to the limitations of the instruments used in the investigation, the TG/DSC data could not be recorded above 1000 $^\circ\text{C}$. The reaction mechanism of Ba₂SnO₄ was well described in literature and suggests that the reaction between the raw materials takes place by equation given below [15];



The primary difference between the TGA curve of B2LS0 and B2LS2 is additional weight loss of 6.37 % in B2LS2, which may be attributed to the hygroscopic aspect of La₂O₃ [31]. The DSC curve of each sample shows an endothermic peak present at 828 $^\circ\text{C}$ and 830 $^\circ\text{C}$ in sample B2LS0 and B2LS2 respectively. The appearance of an endothermic peak in each sample

indicates the initiation of a reaction between the raw materials. The reaction between the reactants is expected to proceed in the same manner as B2LS0;



The weight loss has been calculated from equation (1) and (2) are almost 16.03 %. The weight loss occurred up to 100 °C in B2LS2 is assigned to the evaporation of water molecules adsorbed at the surface of particles that adsorbed during the mixing of solids [32]. Since CO₂ loss is the primary cause of weight loss in both samples, and the total weight loss obtained experimentally is nearly half of what is predicted. The huge difference between experimental and theoretical weight loss suggesting that the decomposition of BaCO₃ does not takes place completely because the reaction not only depends on temperature but also on time. Furthermore, the presence of a weak endothermic reaction peak about 830 °C in the DSC curves of both samples suggests that the reaction begins before complete decomposition of BaCO₃. The presence of reaction peak was in well agreement with the earlier study [33]. Since the amount of doping was quite low, so no significant changes have been observed in present investigation except the hygroscopic properties of La. Therefore, to obtain the phase pure powder the mixture of raw materials should be calcined at 1000 °C for 6 h.

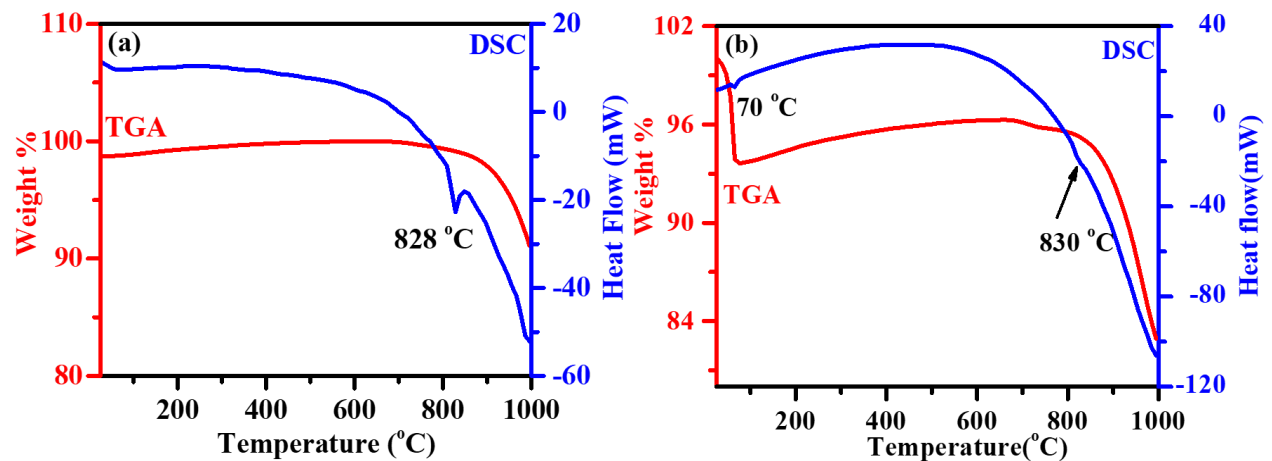


Fig. 1: Thermogravimetric and differential scanning calorimetry curve of prepared mixture of sample (a) B2LS0, (b) B2LS2.

4.2. Determination of phase and crystal structure:

The phase and crystal structure of the prepared samples were determined using powder X-ray diffraction (XRD) analysis. The XRD pattern of calcined powders has been recorded within the angular range 25-80° and shown in Fig. 2. All the diffraction peaks observed in XRD pattern are fine and sharp, suggesting that the sample is crystalline. In order to determine the phase of the sample, the experimental XRD pattern is compared to the JCPDS database and found to be

very similar to the JCPDS file (no- 43-0071) of parent phase Ba_2SnO_4 [34]. It has also been observed that as La is incorporated into the lattice, the size and width of the peaks gradually alter. A new XRD peak (denoted by *) at 27.72° , which belongs to the pyrochlore phase $\text{La}_2\text{Sn}_2\text{O}_7$ (JCPDS card #73-1686), is observed as the concentration of La increased above $x=0.04$. The other pyrochlore phase XRD peaks are located at 35.12° , 51.88° , and 62.46° , which are almost identical to the XRD peak of Ba_2SnO_4 . The intensity of this peak steadily increases, with increasing La. The amount of pyrochlore phase has been estimated using the reference intensity ratio method and found to be approximately 2% for sample B2LS6 and 6% for sample B2LS10. This means that the solubility of La at the Ba site of Ba_2SnO_4 is between 0.04-0.06 weight %. Ba_2SnO_4 is made up of a perovskite BaSnO_3 and a rock salt layer of BaO, meaning that the number of Ba sites is greater than that of BaSnO_3 . The solubility limit of La is found to be close to the La-doping in alkaline perovskite oxides [30,31,35]. This indicates that while there are more sites in Ba_2SnO_4 than in BaSnO_3 , the La is only occupying the sites that are available in BaSnO_3 . In order to understand such behaviour theoretical study must be needed.

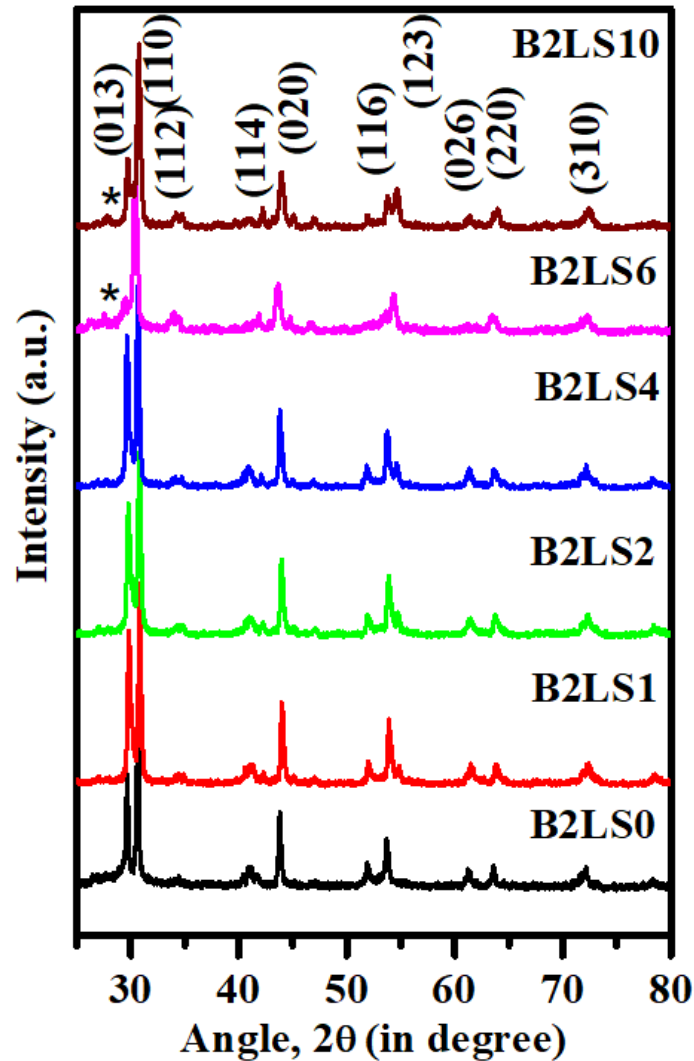


Fig. 2: X-ray diffraction (XRD) pattern of all samples obtained at room temperature.

4.2 Fourier transform infrared (FTIR) Spectroscopy analysis:

Fourier transform infrared (FTIR) spectrum analysis is used to identify the presence of various functional groups in samples, as shown in Fig. 3 (a). The FTIR spectra of all samples are similar to the FTIR spectra of pure Ba_2SnO_4 reported in literature [22]. The FTIR spectra shows bands at 518 cm^{-1} , 623 cm^{-1} , 850 cm^{-1} , 1020 cm^{-1} , 1122 cm^{-1} , 1419 cm^{-1} , 1952 cm^{-1} and a wide band $2424\text{--}3645\text{ cm}^{-1}$ in B2LS0. However, the addition of La to the sample suppressed a few of the bands (1020 , 1122 , 1952 cm^{-1}) and moved the other bands to higher wavenumbers. The vibrations of BaO and SnO_6 octahedra are assigned to the two bands present at 515 cm^{-1} and 616 cm^{-1} , respectively [32,36]. The expand view of the characteristic band has been shown in Fig. 3 (b) in order to describe the incorporation of La into the lattice. The bands present at 515 cm^{-1} shifts towards higher wavenumber while the position of 623 cm^{-1} unchanged with incorporation of La. In terms of effective reduced mass and bond length, this difference can be

explained. The following equation demonstrates a straightforward understanding of this variance;

$$\vartheta = \frac{1}{2\pi} \sqrt{\frac{K}{\mu}} \quad (3)$$

Where K is a constant considered to be as effective bond length and μ is the reduced mass of band arrangement. Since La has a higher mass than Ba, the reduced mass decreases as La is incorporated, resulting in a higher wavenumber needed to vibrate the specific band. Besides these characteristics bands, few more bands are observed at 856, 1024, 1120, 1450, 1936 cm^{-1} assigned to the physically adsorbed $-\text{CO}_2$ and the bands at 1936 and 3294 cm^{-1} is assigned to the adsorbed $-\text{OH}$ at the surface of the sample [36]. It is noticed that with increasing the concentration of La at the Ba site above $x=0.04$, a weak XRD peak belongs to phase $\text{La}_2\text{Sn}_2\text{O}_7$ is appeared in XRD pattern. However, the vibrational band associated with $\text{La}_2\text{Sn}_2\text{O}_7$ is observed within the wavenumber range 550 to 680 cm^{-1} [37]. So, the identification of the pyrochlore phase present in the sample can't be done using this analysis. Therefore, the identification of pyrochlore phase is further analyzed using Raman spectroscopy and discussed in susequent section.

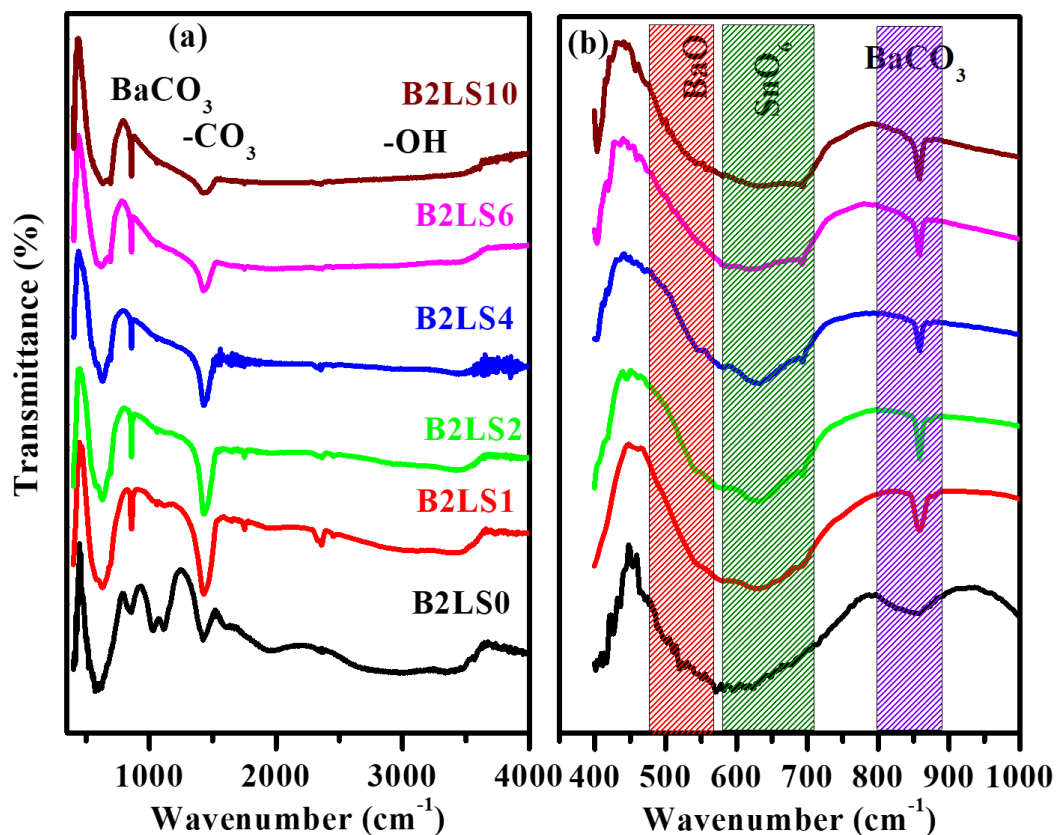


Fig. 3 (a) Fourier transform infrared (FTIR) spectra of prepared samples (b) Enlarge view of FTIR spectra obtained within 400-1000 cm^{-1} .

4.3 Raman Spectroscopy analysis:

Raman spectroscopy is a novel non-destructive and more sensitive technique in comparison with XRD, that usually revealed the local structural information of material [36]. It has piqued interest because of its ability to detect structural changes that alter crystal symmetry at the submicron scale, as well as provide an estimation of the factors that cause these structural changes. Fig. 4 illustrates the Raman spectrum of all samples recorded at room temperature within the wavenumber range 100-1000 cm^{-1} . Raman spectrum of the synthesized samples is compared with the Raman spectrum of K_2NiF_4 type layered perovskite materials [15]. Theoretical calculation revealed that the A_2BO_4 type structures have total 14 optical modes, and among them only 4 modes were found to be Raman active. In A_2BO_4 type structure, B atom was shared by 6 oxygen (4 equatorial oxygen O1 under D_{2h} symmetry and two apical oxygen O2 under C_{4v} symmetry) while 9 oxygens were shared by atom A. The rock salt A-O is connected with the perovskite through apical oxygen along c-direction. The AO_9 dodecahedral involves four equatorial oxygen O2 at same position Z and one apical oxygen along c direction and also four O1 at $z=0$ as shown in Fig. 4. The 14 optical modes have been obtained by the contribution of phonon associated with various atoms are given below;

$$A \rightarrow C_{4v} \rightarrow A_{1g} + E_g + A_{2u} + E_u$$

$$B \rightarrow D_{4h} \rightarrow A_{2u} + E_u$$

$$O(1) \rightarrow D_{2h} \rightarrow A_{2u} + B_{2u} + 2E_u$$

$$O(2) \rightarrow C_{4v} \rightarrow A_{1g} + E_g + A_{2u} + E_u$$

$$\Gamma = 2A_{1g} + 2E_g + 4A_{2u} + 5E_u + B_{2u}$$

Among 14 optical modes only four modes are Raman active (two A_{1g} and two E_g), while experimentally more than four modes are found to be active in present samples [15,38]. The various Raman bands observed in the synthesized sample are assigned to different modes and listed in Table 1. The band appeared at 562 cm^{-1} is characteristic band, that present due to the vibration of oxygen atom within the different plane such as O_x , O_y , and O_z . The nature of this band showing slight asymmetry due to crystal structure of Ba_2SnO_4 ($a = b \neq c$). This characteristic band shows systematic shift towards higher wavenumber due to variation in structural parameters and effective mass. The structural characterization section shows that the substitution of La compressed the all three directions and decreases the net reduced mass. So, this may be a possible reason to observed the shift in position of Raman band towards higher wavenumber (See equation (3)). It is further noticed that a new Raman band is appeared at 597 cm^{-1} for samples B2LS6 and B2LS10 because of the presence of pyrochlore phase ($\text{La}_2\text{Sn}_2\text{O}_7$)

present in sample. The Raman study is completely agreed with XRD analysis, that further reconfirm that the solubility La is limited into the lattice between $0.04 < x \leq 0.06$ weight %.

Table 1: The assignment of different Raman Bands observed in Fig. 5.

Peak notation	Peak position (cm ⁻¹)						Assignment	In Fig. 5a
	B2LS0	B2LS1	B2LS2	B2LS4	B2LS6	B2LS10		
E_g	133.20	136.20	134.73	136.59	147.81	147.81	Vibration of Ba-O2 in ab plane	ν_1
	150.62	155.87	164.80	155.87	177.22	179.89	Vibration of Ba-O1 in ab plane	ν_1'
A_{1g}	194.65	202.15	227.22	188.65	209.18	254.22	Vibration of Ba-O2 along c-axis	ν_2
E_g	299.18	304.36	293.06	296.65	252.89	338.27	Vibration of O2 of SnO ₆ octahedra in ab plane	ν_3
	331.18	333.29	327.07	333.29		401.99	Vibration of bridging oxygen in Ba-O2-Ba in ab-plane	ν_3'
	440.71	443.21	456.45	449.00	472.87	472.87	Second order band	*
A_{1g}	559.46	564.71	565.92	562.78	572.55	578.55	Vibration of oxygen O2 of SnO ₆ along c-axis	ν_4
					597.49	597.49	Vibration of La ₂ Sn ₂ O ₇	@
	687.46	691.89	683.72	691.98	700.14	698.90	Presence of BaCO ₃ at the surface	*

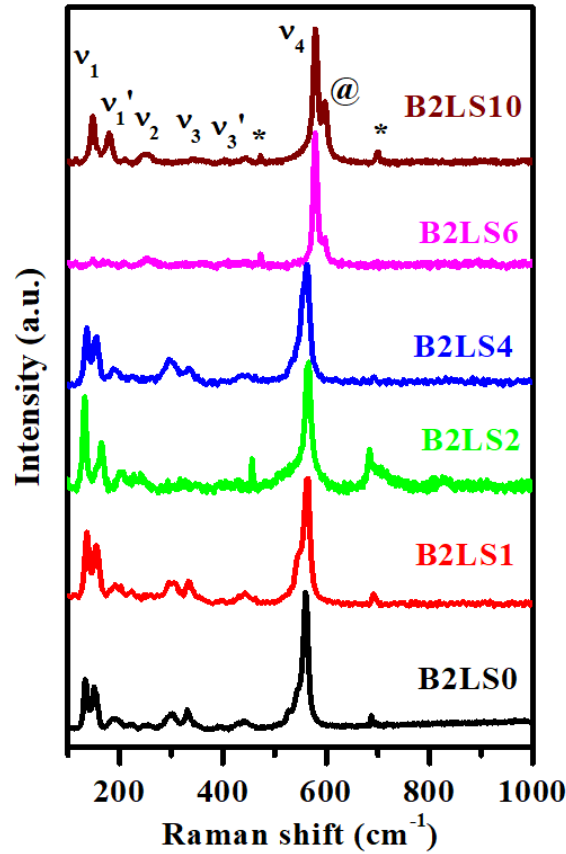


Fig. 4: Raman spectra of prepared samples obtained at room temperature.

4.4 UV-absorption spectroscopy:

The UV absorption spectrum of all the compositions have been recorded within the wavelength range 200-800 nm and shown in Fig. 5. The spectrum shows an intense absorption in UV-region (370-440 nm). The value of absorption wavelength was determined by extrapolating their absorption to the wavelength axis and found to be 375 nm, 392 nm, 394 nm, 430 nm, 399 nm and 395 nm respectively for samples B2LS0, B2LS1, B2LS2, B2LS4, B2LS6 and B2LS10. With the addition of La, the absorption peak shifts to a higher wavelength, which may be due to an inter-shell transition from the energy level of La [36]. The magnitude of absorption varies with La within the UV-region, which could be utilized as metastable state for UV-detector application.

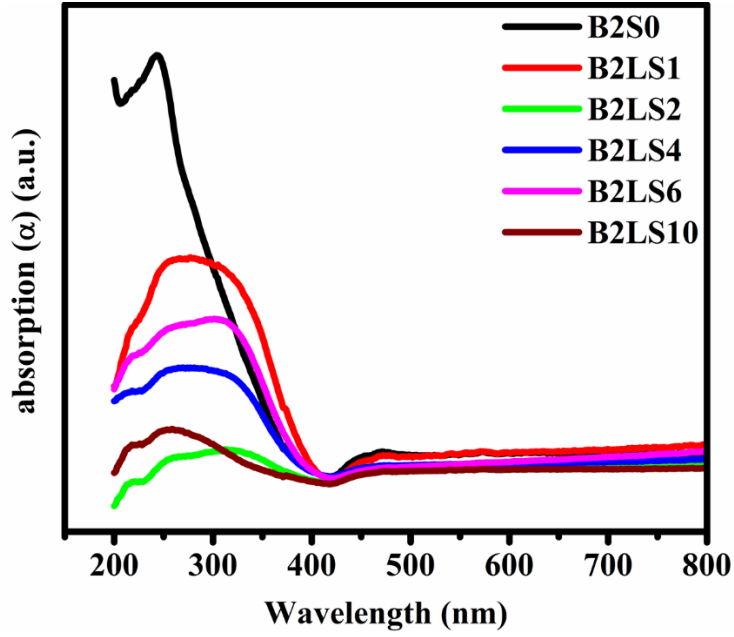


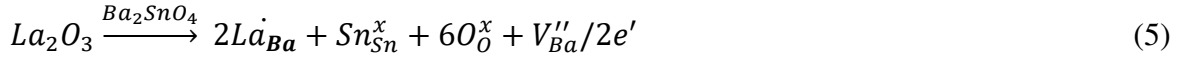
Fig. 5: Ultra-violet (UV) vis spectra of all samples obtained at room temperature.

The optical band gap of the samples is determined from UV absorption data using Tauc relation given by [39]:

$$(\alpha h\nu) = B(h\nu - E_g)^m \quad (4)$$

Where α is the absorption coefficient, $h\nu$ is the energy of photon, B is an energy independent constant, E_g is the energy band gap of the material and m is known as index parameter, which decides the nature of transition. Based on available literature, four values of m is possible such as 2, 3/2, 1, and 1/2 for indirect allowed (indirect band gap) and indirect forbidden, direct forbidden and direct allowed (direct band gap) electronic transition respectively [40]. The direct band gap results due to transition of photon from the bottom of conduction band to top of valence band whereas indirect band gap results due to transition of photon from the intermediate energy states such as defects [41]. The Tauc plot is generated using equation (4) for both direct and indirect band gap of the samples by plotting $(\alpha h\nu)^2$ and $(\alpha h\nu)^{1/2}$ at y-axis and energy of photon ($h\nu$) at x-axis and shown in Fig. 6. Extrapolating the linear portion of the curve to the x-axis provides the direct and indirect band gap values. The values of direct band gap for undoped sample obtained in this work is in agreement with the values reported in the literature [42,43]. The value of direct bandgap was found to be 3.75 eV, 3.23 eV, 3.28 eV and 3.30 eV and indirect bandgap to be 3.26 eV, 2.92 eV, 3.04 eV and 3.05 eV for samples B2LS0, B2LS1, B2LS2 and B2LS4 respectively. However, as XRD and Raman analysis indicate that the presence of pyrochlore phase in sample B2LS6 and B2LS10, the UV-Vis spectra also

reflect two bandgap one is may be of B2LS composition and other for pyrochlore phase. In present case, the discussion for sample B2LS6 and B2LS10 excluded due to presence of pyrochlore phase and solubility limit of La into the lattice. One major change has been observed that the direct bandgap and indirect bandgap of the La-doped samples are found to be lower than undoped. In order to understand this variation, the charge compensation mechanism has been taken into account. Since La acts as donor for Ba-site and the charge compensation mechanism takes place by following equation;



Since the samples are synthesized at high temperature, so the loss of oxygen can't be ruled out and given by;



The position of defect state $2L\dot{a}_{Ba}$ formed below the conduction band that might be one of the possible reasons for decreasing the bandgap. However, as La is increased, the concentration of defect state $2L\dot{a}_{Ba}$ increases, since this defect has a positive charge and as its concentration increases, a small amount of columbic repulsive force between defect states acts, which may be an explanation for the bandgap rising. Moreover, the presence of indirect bandgap in samples suggests the presence of defect such as oxygen vacancy (see equation (6)) [33,44]. Since the difference between the direct and indirect bandgap has been found to be 0.49 eV, 0.31 eV, 0.24 eV and 0.25 eV for samples B2LS0, B2LS1, B2LS2 and B2LS4 respectively. Since the value of difference has been decreased with La, that might be due to increase of oxygen vacancy. The value of direct bandgap reflects inorganic semiconducting nature of samples, and utilized it for semiconductor device application.

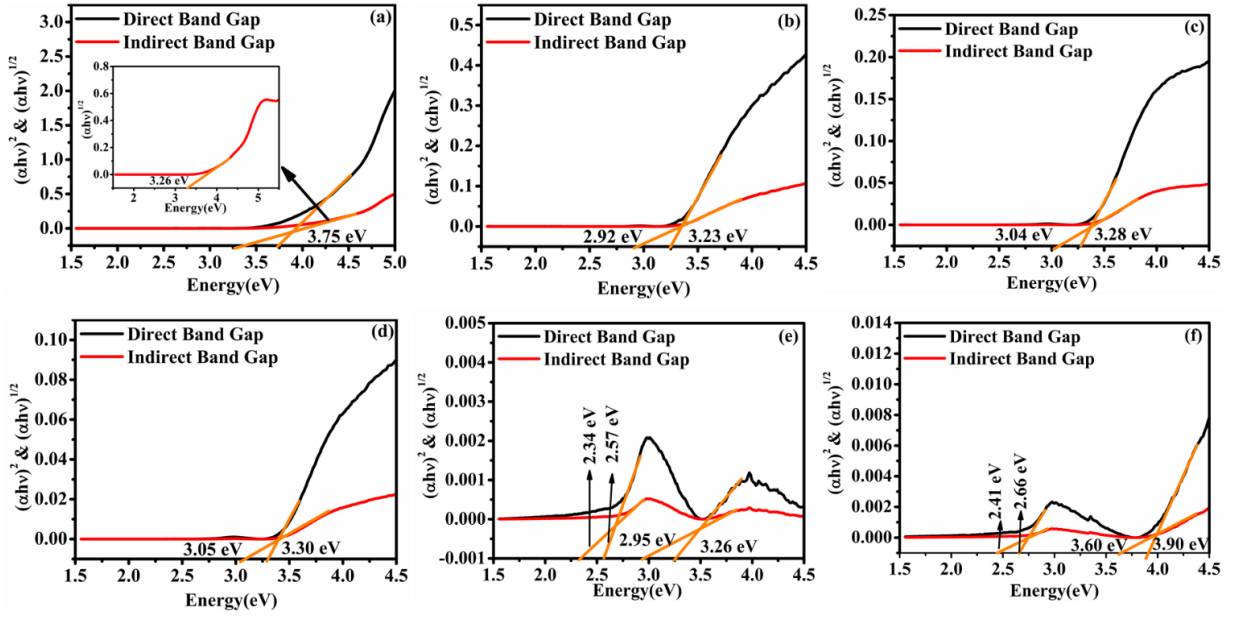


Fig. 6: Tauc's plot generated for direct and indirect band gap of all samples.

3.3. Morphological studies of sintered pellets of system $(\text{Ba}_{1-x}\text{La}_x)_2\text{SnO}_4$

To study electrical and morphological properties of the synthesized samples, calcined powders of all the compositions have been pelletized and sintered at 1250 °C for 6 h. For microstructural studies freshly fractured surfaces of the sintered pellets were coated with gold using sputtering unit. The Field emission scanning electron micrograph (FESEM) of the fractured surface of the samples have been recorded and shown in Fig. 7. From Fig. 7, it has been noticed that the grains are agglomerated and spherical in shape. However, the degree of agglomeration among the grains reduces with La. Further, the value of average grain size for all samples have been calculated using 'Image J' software. Initially, the histogram between the number of grain and their size has been generated for all samples and shown in the inset of each figure of Fig. 7. In order to determine the average grain size, the Gaussian distribution function has been fitted to the histogram and the value of grain size is given in the Fig 7. It has been further noticed that the value of average grain size is decreased with increasing concentration of dopant. Since La^{3+} at Ba^{2+} site of Ba_2SnO_4 act as a donor and charge neutrality may be maintained by equation (5). As the concentration of La in the Ba_2SnO_4 increases the concentration of either electron or V''_{Ba} increases. It is well reported in literature that the donors act as grain growth inhibitor whereas oxygen vacancies promotes the grain growth process [45]. This might be possible reason for the variation of grain size observed in present samples.

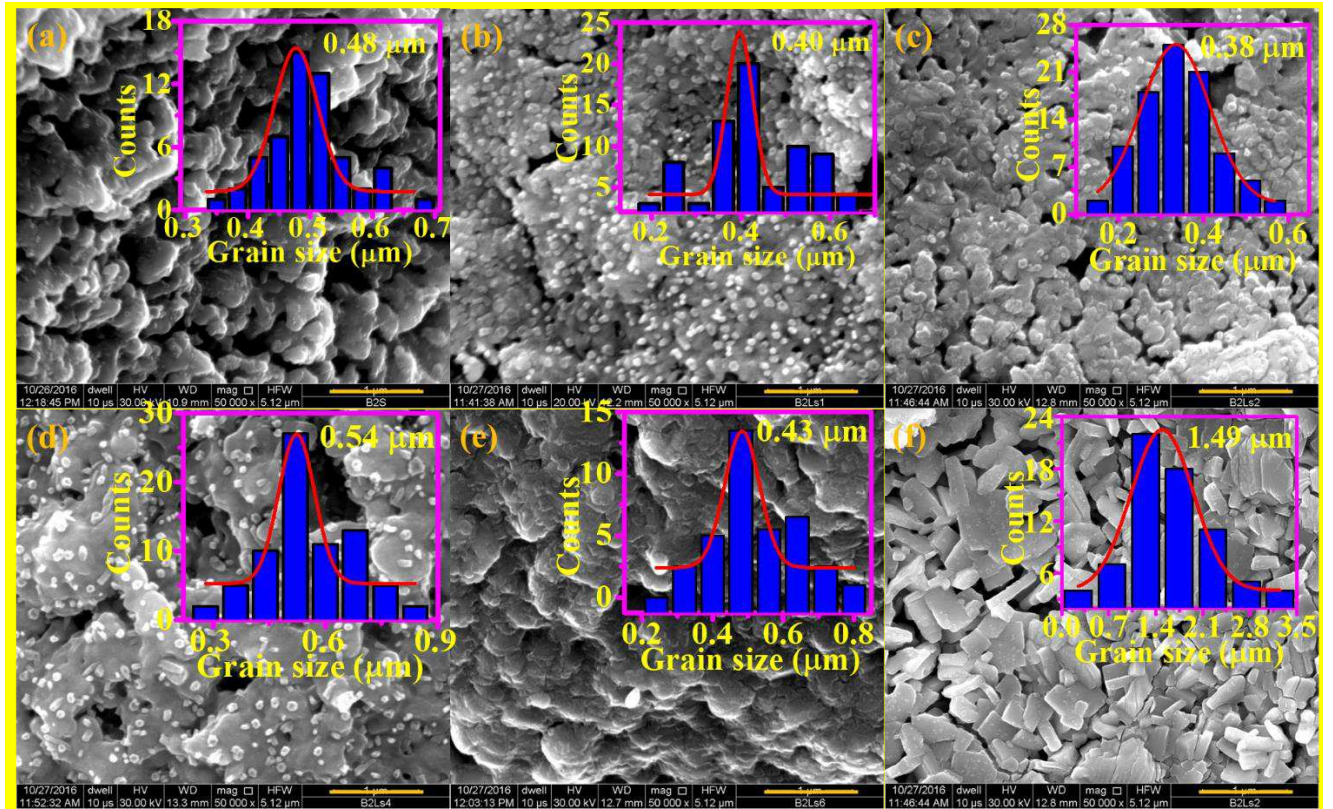


Fig. 7: Field Emission Scanning Electron Micrograph (FESEM) of the fractured surface of sintered samples (a) B2LS0 (b) B2LS1 (c) B2LS2 (d) B2LS4 (e) B2LS6 (f) B2LS10.

3.3 Characterization of Single-phase powders of $(\text{Ba}_{1-x}\text{La}_x)_2\text{SnO}_4$ system

3.3.1 Reitveld profile analysis:

Structural parameters of the single-phase samples have been determined using Reitveld refinement analysis performed on powder X-ray diffraction data. The refinement has been performed using FullProf software suite by adopting crystal structure as tetragonal with space group (#139, I4/mmm). The peak function has been modelled as Pseudo-Voigt (A combination of Lorentzian and Gaussian function) given by;

$$P.V. = \eta * L + (1 - \eta) * G \quad (7)$$

Where, η , L , G are the positive constant, contribution of Lorentzian and Gaussian function present in XRD peak respectively. The background for the XRD diffraction pattern has been described in terms of 12th order polynomial function [46]. The refinement has been processed until the achievement of best fit. The Reitveld refined pattern of single-phase solid solutions are shown in Fig. 8(a). The quality of fitting has been judged by calculating a parameter S using weighted profile pattern (R_{wp}) and pattern profile (R_p) through formula, $S = R_{wp}/R_p$. The value of S for all samples found to be unity suggests that the parameters derived from

refinements are relevant. The refined parameters along with other relevant structural parameters such as most affected bond length and bond angles are given in [Table 2](#).

Table 2: Lattice Parameters, Position parameters, Refinement parameters, Bond length, Bond angle, Crystallite size and micro-strain of all samples.

Parameters	B2LS0	B2LS1	B2LS2	B2LS4
Lattice Parameters				
a=b	4.1458	4.1419	4.1418	4.1413
c	13.2899	13.2950	13.2859	13.2915
Volume	228.42	228.08	227.91	227.95
X-ray density (g/cm ³)	7.53	7.036	6.68	6.59
Position Coordinate				
Ba	(0,0,0.35235)	(0,0,0.35036)	(0,0,0.35268)	(0,0,0.34830)
La	--	(0,0,0.35036)	(0,0,0.35268)	(0,0,0.34830)
Sn	(0,0,0)	(0,0,0)	(0,0,0)	(0,0,0)
O1	(0.5,0,0)	(0.5,0,0)	(0.5,0,0)	(0.5,0,0)
O2	(0,0,0.13636)	(0,0,0.14111)	(0,0,0.15390)	(0,0,0.16091)
Refinement Parameters				
Rp	10.5	10.6	12.5	8.3
Rwp	11.8	11.4	13.1	9.6
Re	13.03	8.4	9.01	9
χ^2	3.72	5.5	6.1	5.6
S=R _{wp} /R _p	1.12	1.07	1.05	1.15
Bond Length				
Ba-Sn	3.5577	3.5275	3.5125	3.5053
Ba-O1	2.8544	2.8495	2.8368	2.8302
Ba-O2	2.9354	2.9341	2.9321	2.9303
Sn-O1	2.0729	2.0728	2.0709	2.0706
Sn-O2	1.8122	2.1305	2.1447	2.1600
Bond Angle				
O2-Ba-O2 (layer)	176.14	176.74	176.88	177.00
Ba-O1-Ba (Perovskite)	86.859	86.799	86.669	86.477

Crystallite size (nm)	24.47	18.84	17.52	16.48
Micro-Strain ($\times 10^{-3}$)	2.91	3.89	4.91	6.06

From Table 2, it has been noticed that the value of lattice parameters (a, b) found to be decrease while parameter c shows random variation. However, the volume of unit cell and x-ray density found to be decrease with incorporation of La into the lattice. Further, the different bond lengths Ba-Sn, Ba-O1, Ba-O2 and Sn-O1 were also found to be decrease with La that supports the experimental results. The variation in these structural parameters were found due to difference in ionic radii of dopant La^{3+} (1.21 Å) to host Ba^{2+} (1.44 Å) [47]. The crystal structure of a reference sample has been generated using crystallographic information file (CIF) through the **Vesta Software** and shown in Fig. 8(b). In the crystal structure, the perovskite (BaSnO_3) is sandwiched between two adjacent rock salt layers (BaO). The position coordinate of the atoms was already given in Table 2, that indicates that with incorporation of La, the z-coordinate of Ba and O2 shifted from their mean position. In this figure the number of unit cell along a,b-axis is higher compared to c-axis, that might be a possible reason that the solubility of La at Ba-site takes place similar to the perovskite BaSnO_3 . As La occupied the sites available in lattice, the charge compensation mechanism takes place by equation (5) so the resultant charge may create lattice strain due to which small shift is observed in the position of O2 along x-axis. This shift may apply a small amount of force on Ba present in layer and perovskite that could be seen from angle (O2-Ba-O2) and (Ba-O1-Ba). Further the effect of doping also studied in terms of micro-strain in subsequent section.

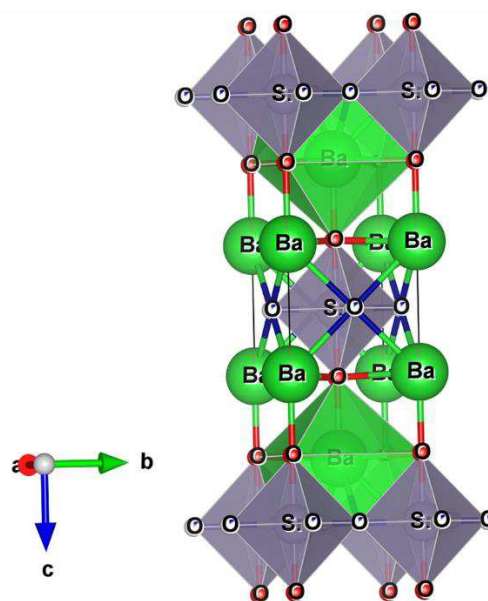
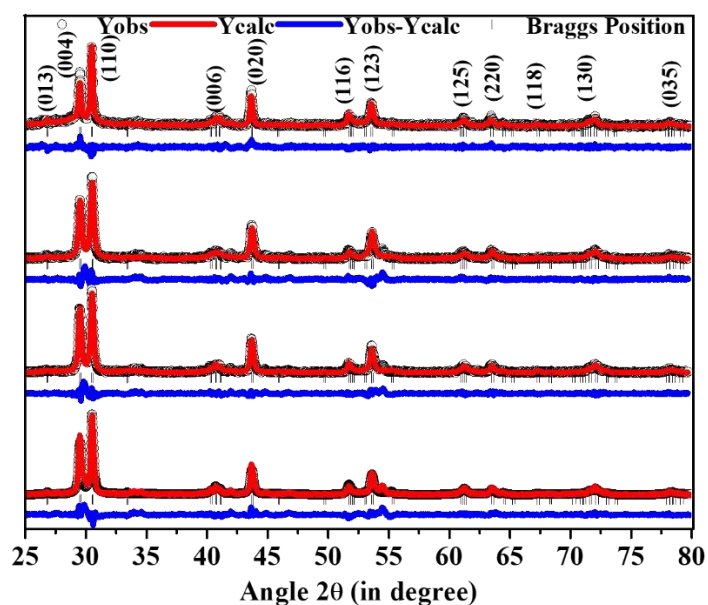


Fig. 8 (a) Rietveld refinement pattern of all samples, (Yobs, Ycalc, Yobs-Ycalc, and Bragg's position represent experimental pattern, calculated pattern, difference between experimental and calculated pattern, and Bragg's diffraction peaks respectively). **(b)** Crystal structure of a reference sample generated after refinement.

Electrical Properties Measurement

The electrical properties of silver coated pellets have been measured as a function of frequency (20 Hz-2 MHz) and temperature range 300-600°C. The frequency dependence conductivity for many polycrystalline, ceramics, glass-ceramics etc. have been well explained by Jonscher's power law given by A. K. Jonscher's in 1978 expressed mathematically in following form;

$$\sigma(\omega, T) = \sigma_{dc} + B\omega^s(T) \quad (8)$$

Where, B is a temperature dependent constant, s is power exponent parameter which usually lies in between 0 to 1, ω is angular frequency $\omega = 2\pi f$, and f is angular frequency. The Jonscher's power law has been further modified as [46];

$$\sigma(f, T) = \sigma_{dc} \left[1 + \left(\frac{f}{f_h} \right)^s \right] \quad (9)$$

In above equation $f_h = \left(\frac{\sigma_{dc}}{B} \right)^{1/s}$, and the parameter s is an important parameter called as power exponent that usually lies between $s = 0$ to 1 such that $s = 0$ indicates frequency independent region (linear plateau parallel to frequency axis) called as dc conductivity (σ_{dc}), and $s = 1$ indicates frequency dependence of conductivity. Frequency dependence of ac conductivity for all samples were depicted in Fig. 9 (a) for a reference sample B2LS2. Since the frequency dependence of ac conductivity for rest samples are similar to B2LS2 with only change in their magnitude so their plots have been given in supplementary file. The value of σ_{dc} , f_h and s were obtained at each temperature by employ fitting of equation (9) to experimental data, shown by solid line in each figure.

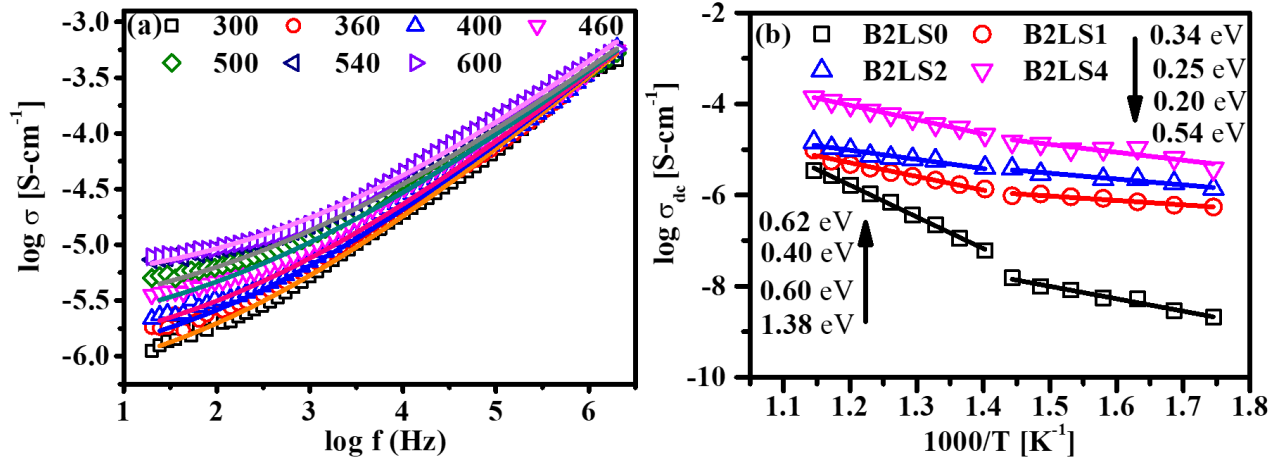


Fig. 9: Variation of ac conductivity as a function of frequency, (a) B2LS2, (b) thermal dependence of dc conductivity for all samples. (Symbols shows the experimental data point and solid line shows fitted data).

The thermal dependence of dc conductivity has been shown in Fig. 9 (b), to study about the conduction mechanism operative in samples. Arrhenius model gives a relation between the dc conductivity and temperature by following relation [7];

$$\log \sigma_{dc} = \log \sigma_o + \left(-\frac{E_{cond.}}{k_B T} \right) \quad (10)$$

Where, σ_o is preexponential factor, k_B is Boltzmann constant and $E_{cond.}$ is activation energy for the migration of charge species within the samples. The activation energy of each samples has obtained by fitting of equation (10) to experimental data as shown by solid line. The thermal dependence dc conductivity curve shows two regions with different value of activation energy as mentioned in each fig. The conduction mechanism of undoped sample was already reported in literature, therefore, here only it has been considered as reference [15]. The activation energy for undoped samples found to be 1.38 eV (high-temperature region) and 0.54 eV (low temperature region), and with incorporation of La, the activation energy in both regions were decreased, while dc conductivity was increased. This variation can be understood in terms of charge compensation mechanism given by equation (5). Since the doping of La at Ba-site leads to an excess positive charge ($2La_{Ba}'$) that can be compensated either by creation of electron (e') or V''_{Ba} . The dc conductivity of doped sample increases with doping concentration of La suggest that the excess of positive charge on lattice compensated by generation of electron to maintain the overall charge neutrality. Further, the detailed conduction mechanism has been explored in further section.

In order to understand about the relaxation mechanism in depth, the logarithmic of hopping frequency (f_h) has been plotted with respect to inverse of temperature and shown in Fig. 10. The activation energy for relaxation process ($E_{relax.}$) has been calculated using similar equation to Arrhenius equation that is given by [48];

$$\log f_h = \log f_o + \left(-\frac{E_{relax.}}{kT} \right) \quad (11)$$

Where, f_o is preexponential factor, and k is Boltzmann constant. The linear fitting of equation (11) to the experimental data shown by solid line gives the value of $E_{relax.}$. The value of activation energy found highest for undoped and it decreased with incorporation of La similar to dc conductivity.

Since the optical band gap is lowest for sample B2LS1, i.e., 3.23 eV, while the activation energy for all samples were found to be less than the separation between valence band and conduction band, that exclude any type of intrinsic conduction. As the samples were synthesized at high temperature, the presence of oxygen vacancy can't be ruled out and given by equation (6). The electrons present in equation (6) may further reduce the valence states of Sn such as; $Sn^{4+} + 2e' \rightarrow Sn^{2+}$. There are following two ways by which the conduction takes place within samples; (i) either by jumping of electron between the degenerate sites of Sn, (ii) Orientation of electron through dipole ($\vec{V}_o - Sn^{4+}_{Sn^{2+}}''$). Based on available literature, the activation energy found greater or equal to 1 eV assigned to the migration of oxygen vacancy while the activation energy lies in between 0.5 eV to 1 eV assigned to the migration of mixed ionic and electronic (i.e., polaronic) and less than 0.5 eV assigned to the purely electronic conduction [49]. The activation energy obtained from dc conductivity is found to be 1.38 eV, 0.60 eV, 0.40 eV, 0.62 eV in region-1 (High temperature region) and 0.54 eV, 0.20 eV, 0.25 eV, 0.34 eV in region-2 (Low temperature region) for samples B2LS0, B2LS1, B2LS2 and B2LS4 respectively. However, activation energy obtained from hopping frequency is found to be 1.61 eV, 0.52 eV, 0.70 eV, 0.82 eV in region-1 (High temperature region) and 0.51 eV, 0.35 eV, 0.31 eV, 0.44 eV in region-2 (Low temperature region) for samples B2LS0, B2LS1, B2LS2 and B2LS4 respectively. The activation energy derived from dc conductivity and hopping frequency are nearly identical, implying that the origin of conduction and relaxation mechanisms in both processes are the same. The higher value of activation energy is observed for undoped sample may indicates a strong association among the defect dipoles ($\vec{V}_o - Sn^{4+}_{Sn^{2+}}''$), that need small amount of energy initially for dissociation and then it migrates.

The dc conductivity results in high temperature region reflect the ionic migration that transformed to polaronic with incorporation of La, while the low temperature region reflects the electronic conduction that remain same for all samples. Since, the conductivity in undoped samples results due to migration of oxygen vacancy and electron, however, the activation energy gradually decreased with incorporation of La that observed either of decrease in oxygen vacancy or increase of hopping length. The dc conductivity was found to be increased that may be due to either larger charge carrier concentration or higher mobility. Increasing in mobility may also leads to an increase in activation energy that does not support the present result. Therefore, the reason for increasing the dc conductivity is increase of charge carrier concentration. Also, La acts as donor for Ba-site of Ba_2SnO_4 and the overall charge has been compensated by creation of electron as given by equation (5). Due to electronic charge compensation mechanism, the number of electrons within the samples also increase and it results to rise in dc conductivity.

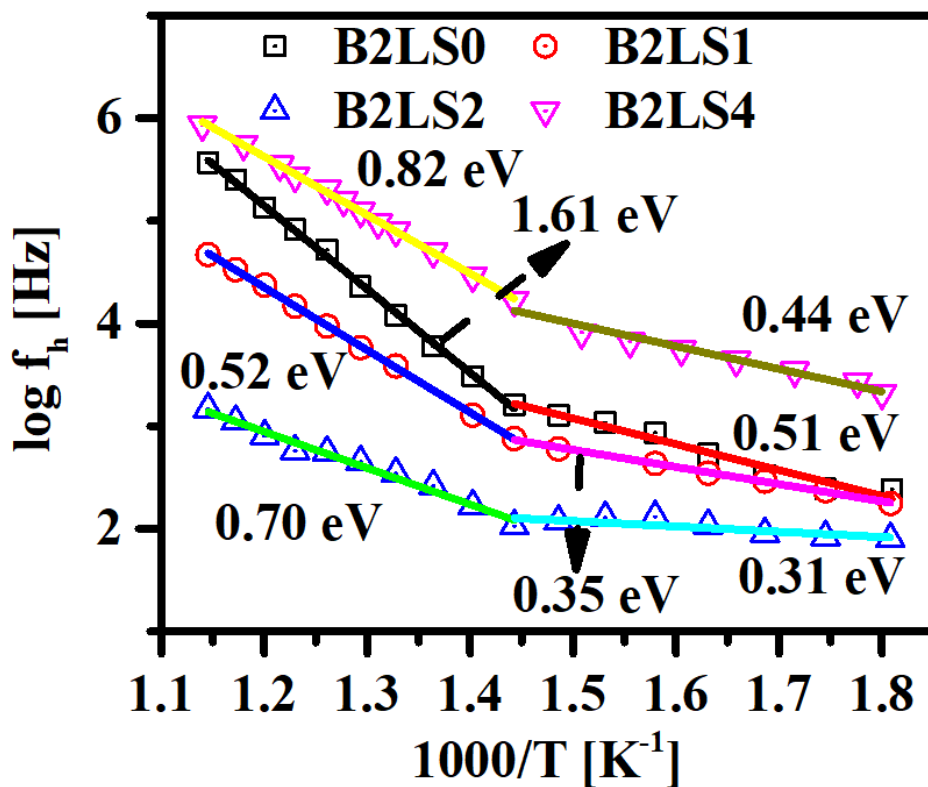


Fig. 10: Thermal dependence of hopping frequency (f_h) for all samples. Symbols show the experimental data point and the solid line represent the fitting of equation (11).

In order to see the role of temperature and composition on conduction and relaxation process occurred in sample; the time temperature superposition principle (TTSP) has been taken into account and given by [50]:

$$\frac{\sigma}{\sigma_{dc}} = F\left(\frac{f}{f_h}\right) \quad (12)$$

The TTSP curve has been generated by scaling the frequency axis (f) with hopping frequency (f_h) and ac conductivity (σ) with dc conductivity (σ_{dc}) at each temperature and shown for sample B2LS1 and B2LS4 in Fig. 11 (a) and (b) respectively. All the thermal curve perfectly superimposes on each other at all temperatures, indicating reflects that the sources of charge carriers are remain same at all temperature. Therefore, the conduction in sample within low temperature region take place via hopping of electron between the degenerate sites of Sn while in high temperature region the conduction take place via orientation of electron from Sn^{4+} to Sn^{2+} through polaron.

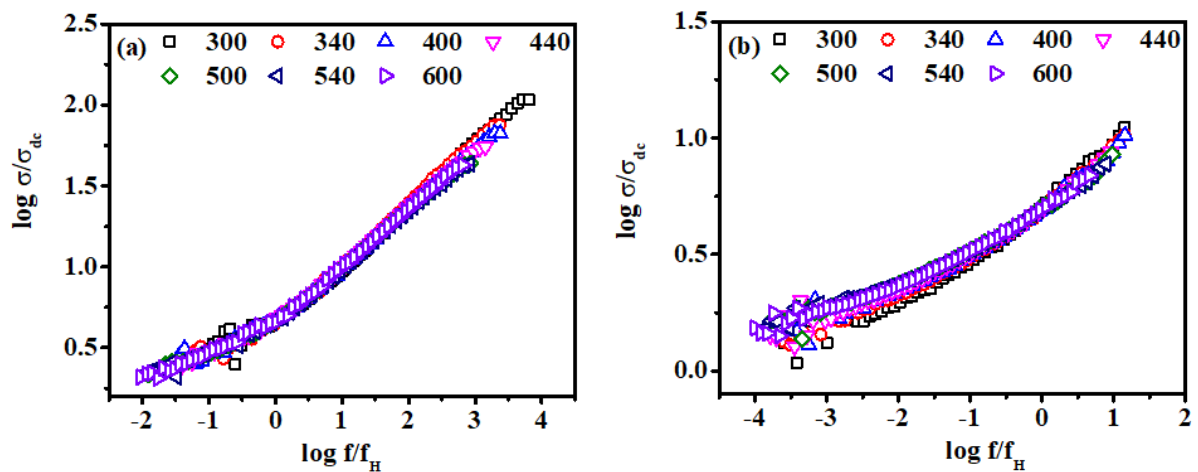


Fig. 11: Time-Temperature Superposition Principle (TTSP) curve for samples, (a) B2LS1 (b) B2LS4.

In order to explore the conduction mechanism, the variation of power exponent as a function of temperature has been illustrated in Fig. 12. The power exponent represents the dimensionality of conduction as well as the strength among the host lattice with the mobile species. Based on the variation of power exponent, different models are well discussed in the literature to explore the ac conduction mechanism involved in the samples [15]. Few of them are given below;

1. Minimum values of s followed by an increase suggests that the conduction in samples occurred by overlapping of large polaron tunneling (OLPT) model.
2. Temperature independent variation of s suggests the occurrence of conduction through Quantum mechanical tunneling (QMT).
3. Decrease of s with temperature suggests the presence of correlated barrier hopping (CBH) in the samples.

Based on the variation observed for power exponent, the OLPT model is most suitable to analyse the detailed ac conduction mechanism in present samples.

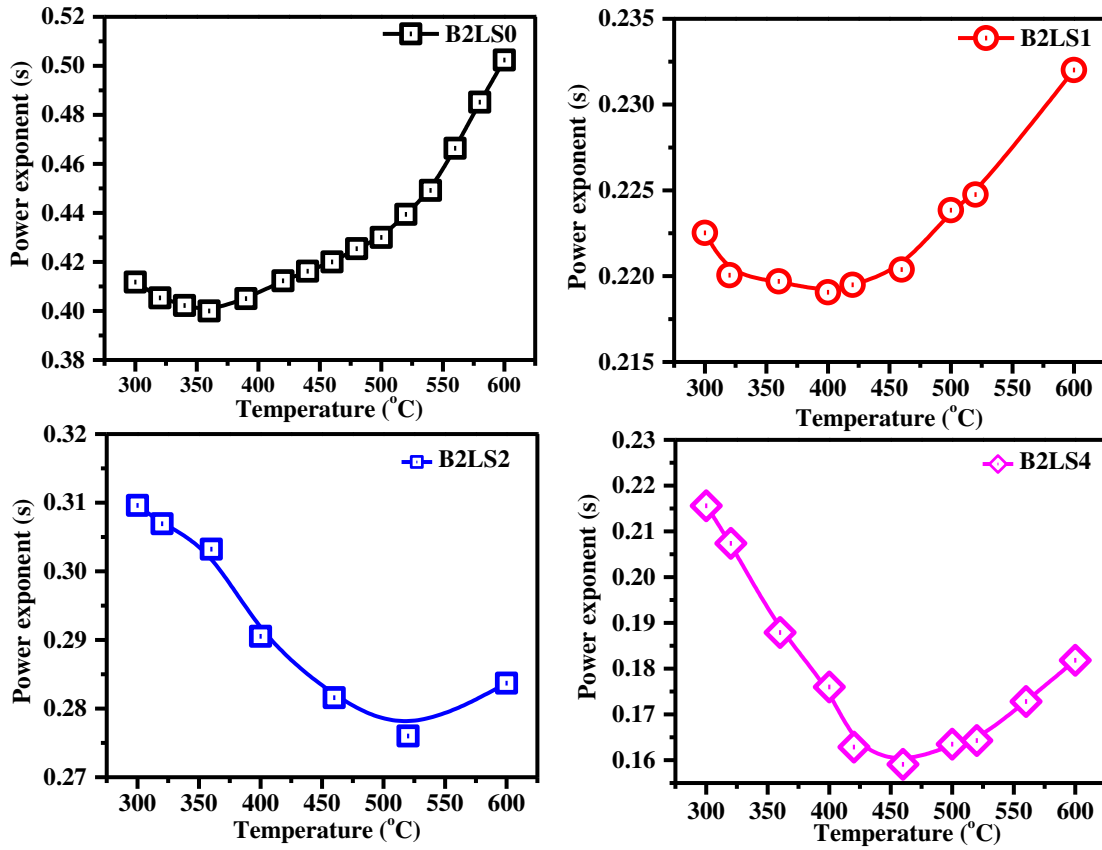


Fig. 12: Variation of power exponent as a function of temperature for all samples.

In OLPT model, the power exponent s depend both on frequency and temperature. Initially s had dropped to a minimum value with increasing temperature and then escalated with further increase in temperature [51]. The ac conductivity in OLPT model is usually given by following equation [52];

$$\sigma_{ac}(\omega) = \left[\frac{\pi^4 e^2 k_B^2 T^2 N^2}{12} \right] * \frac{\omega R \omega^4}{2\alpha k_B T + \frac{W_{HO} r_p}{R \omega^2}} \quad (13)$$

Here, k_B is the Boltzmann's constant, N is the number of defect state near the Fermi level, α is the inverse of localization length, R_ω is the hopping length, W_{HO} is the energy required for overlapping of the polaron and r_p is the length of polaron. The hopping length is further determined by solving the quadratic equation [53];

$$R'_\omega{}^2 + [W_{HO}\beta + \ln(\omega\tau_o)]R'_\omega - W_{HO}r'_p\beta = 0 \quad (14)$$

Where $\beta = 1/k_B T$, $R'_\omega = 2\alpha R_\omega$, and $r'_p = 2\alpha r_p$. Also, the frequency exponent s can be expressed in this model is given by;

$$s = 1 - \frac{8\alpha R_\omega + \frac{6W_{HO}r_p}{R_\omega k_B T}}{\left[2\alpha R_\omega + \frac{W_{HO}r_p}{R_\omega k_B T}\right]^2} \quad (15)$$

Fig. 13 shows the temperature dependence of AC conductivity at constant frequency 10 KHz for all samples. The experimental data were fitted to the equations (12) using $N(E_f)$, W_{HO} , r_p , R_ω , and α as the initial parameters [52]. All the parameters were derived from the least square fitting and given in Table 3.

Table 3: Parameters obtained from OLPT model fitting.

Sample Code	$N(E_f)$ (x 10^{19}) ($\text{ev}^{-1}.\text{cm}^{-3}$)	α (\AA^{-1})	r_p (\AA)	R_ω (\AA)	W_{HO} (eV)
B2LS0	1.44	0.220	0.836	3.62	1.06
B2LS1	2.06	0.219	0.940	3.59	0.86
B2LS2	3.14	0.192	1.092	3.53	0.65
B2LS4	4.56	0.195	1.061	3.27	0.43

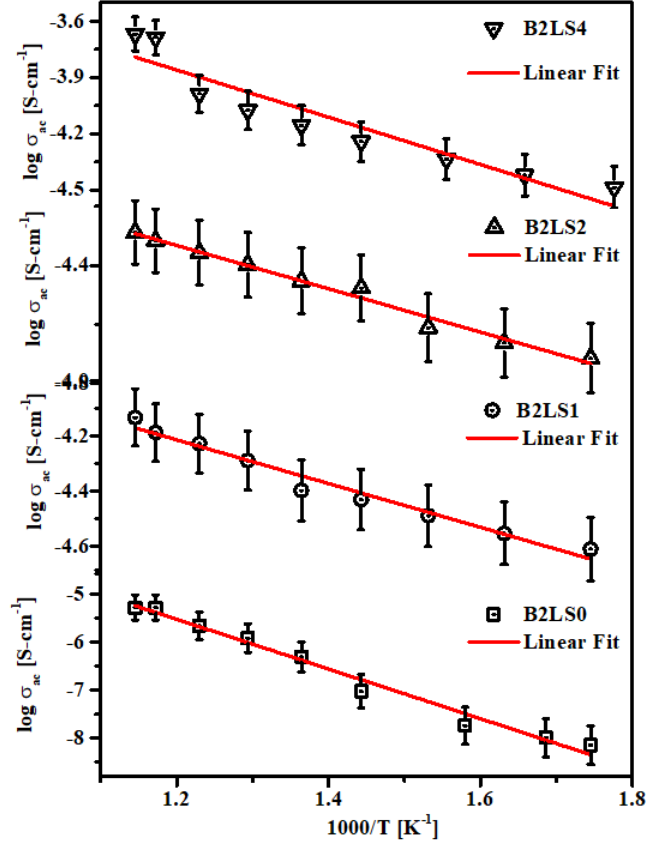


Fig. 13: Variation of power exponent (s) with respect to inverse of temperature. Symbols shows experimental data and solid line shows fitted data using equation (13).

From Table 3, it has been noticed that with incorporation of La^{3+} the value of charge carrier concentration increases that might be possible reason for rise in dc conductivity. It is also clear that the value of hopping length (R_ω) decreases with La^{3+} , that follow similar trend of the interatomic distance given in Table 2 such as Ba-O1 = 2.89019-2.8544 (Å), Ba-O2 = 2.9354-2.9303 (Å), Sn-O1 = 2.06285-2.0729 (Å), and Sn-O2 = 1.8122-2.2605 (Å). Also, it has been noticed that the interatomic distance is found lower than the hopping length that suggests the formation of large polaron. So, the conduction in the sample takes place via formation of the overlapping of large polaron. In case of large polarons, the spatial extent of the polaron is larger compared to the interatomic distance [54]. Since the W_{HO} is the value of activation energy for the hopping of charge carrier between neighbouring sites via the overlapping. The value of W_{HO} obtained for present sample is nearly equal to the activation energy obtained from dc conductivity that further supports the migration of charge carrier between the degenerate sites through overlapping of polaron. Further, the value of polaron radius increases with doping concentration of La^{3+} that need lower amount of energy for the migration of polaron.

As previously mentioned, Ba₂SnO₄ is made up of a perovskite BaSnO₃ and a BaO sheet, so the result of Ba₂SnO₄ can be compared to that of BaSnO₃. BaSnO₃ is crystallized into cubic crystal structure with Ba²⁺ ions in dodecahedral site and Sn⁴⁺ ion is at octahedral site. The distance between the Sn-O and Ba-O were 2.05779 Å, 2.91015 Å respectively [46]. Also, a comparison between the dc conductivity of La-doped BaSnO₃ and with present investigated samples at 600°C has been made [29]. The BaSnO₃ doped with La (1 %) had dc conductivity of 1.41 x 10⁻⁴ S-cm⁻¹ while B2LS1 had a dc conductivity of 1.26 x 10⁻⁵ S-cm⁻¹. Since the conduction in BaSnO₃ is governed by the nearest neighbour site either O-Sn-O or Sn-O-Sn which is remain same in Ba₂SnO₄. Conduction occurs in samples between two lattice sites with lower potential energy through the defect only when the defect relaxes before the two minima of lattice potential energy coincide with the lattice site [55]. Furthermore, the presence of a Ba-O layer exerted pressure on the perovskite BaSnO₃, causing a difference in the crystal structure of BaSnO₃ found in Ba₂SnO₄ and regular BaSnO₃. Furthermore, the interatomic distance of our compounds Sn-O1, Sn-O2 is found to be greater than the interatomic distance of Sn-O in BaSnO₃. As a result of this explanation, we can infer that there is a difference in conductivity between these two compounds. Thus, in the present sample, conductivity is ensured by the overlapping of large polarons within the large tunnels, while in BaSnO₃, it is ensured by the overlapping of small polarons within the small tunnels [56].

Moreover, the contribution of grain, grain boundary, and electrode to the overall electrical properties can be studied using Nyquist plot. The Nyquist plot has been shown in Fig. 14 for all samples obtained at selected temperatures such as 300°C, 400°C, 500°C, and 600°C. A depressed semi-circular arc has been observed for all samples. Further, the Nyquist plot has been fitted with a Cole-Cole equation to determine the contribution of grain and grain boundary is given by [57];

$$\left(Z' - \frac{R}{2}\right)^2 + Z'' = \left(\frac{R}{2}\right)^2 \quad (16)$$

The resistance of grain and grain boundary were determined by employing the equation (16) to experimental data shown by solid line in Fig. 14. Ideally, three semi-circular arcs have been observed that assigned to the grain, grain boundary, and electrode contribution respectively [51]. Although they are found to be present separately not only at higher frequency but also due to large difference in their relaxation time. The measurement cannot be performed at higher frequency due to limitation of instrument used in present investigation. In present sample, only a singular arc has been observed that indicates the resistance can be given by R_{total}=

$R_g+R_{gb}+R_{elec}$. Since the arcs observed in present investigation are depressed that reflects the distribution of relaxation time among the grains/grain boundaries. Further, the SEM analysis shows agglomeration among the grains that might be one of the reasons that the contribution of grain boundaries was not separable. The value of resistance obtained by fitting of cole-cole equation has been given in Table 4. At the top of the semicircle, following condition should be satisfied [57];

$$2\pi f_{max}RC = 1 \quad (17)$$

The value of effective capacitance was calculated using the frequency and resistance at each temperature for all samples and given in Table 4. The value of effective capacitance calculated from equation (17) was found to be in agreement with the effective capacitance arised due to major effect of interface present within the samples [22,58]. Therefore, in order to further study about the role of grain to the electrical conduction and relaxation mechanism, the thermal dependence of effective resistance was taking into account.

Table 4: The value of Resistance, capacitance, frequency (f_{max}) obtained at different temperatures for all samples.

Sample	Temperature (°C)	R_{total} (ohm)	f_{max} (Hz)	C_{total} (F)
B2LS0	300	8.69×10^6	253	4.54×10^{-10}
	400	3.75×10^6	552	4.83×10^{-10}
	500	2.98×10^6	671	5.00×10^{-10}
	600	2.14×10^6	991	4.72×10^{-10}
B2LS1	300	4.70×10^6	307	6.93×10^{-10}
	400	2.93×10^6	671	5.08×10^{-10}
	500	1.24×10^6	990	8.14×10^{-10}
	600	7.84×10^5	1463	8.72×10^{-10}
B2LS2	300	3.32×10^6	453	6.64×10^{-10}
	400	1.97×10^6	815	6.23×10^{-10}
	500	1.14×10^6	1204	7.29×10^{-10}
	600	7.38×10^5	1779	7.62×10^{-10}
B2LS4	300	3.87×10^5	670	3.87×10^{-9}
	400	2.22×10^5	1463	3.08×10^{-9}
	500	1.34×10^5	2162	3.45×10^{-9}
	600	8.60×10^4	3194	3.64×10^{-9}

The conduction mechanism of charge carrier within grain has been discussed by determining the grain resistance for all samples.

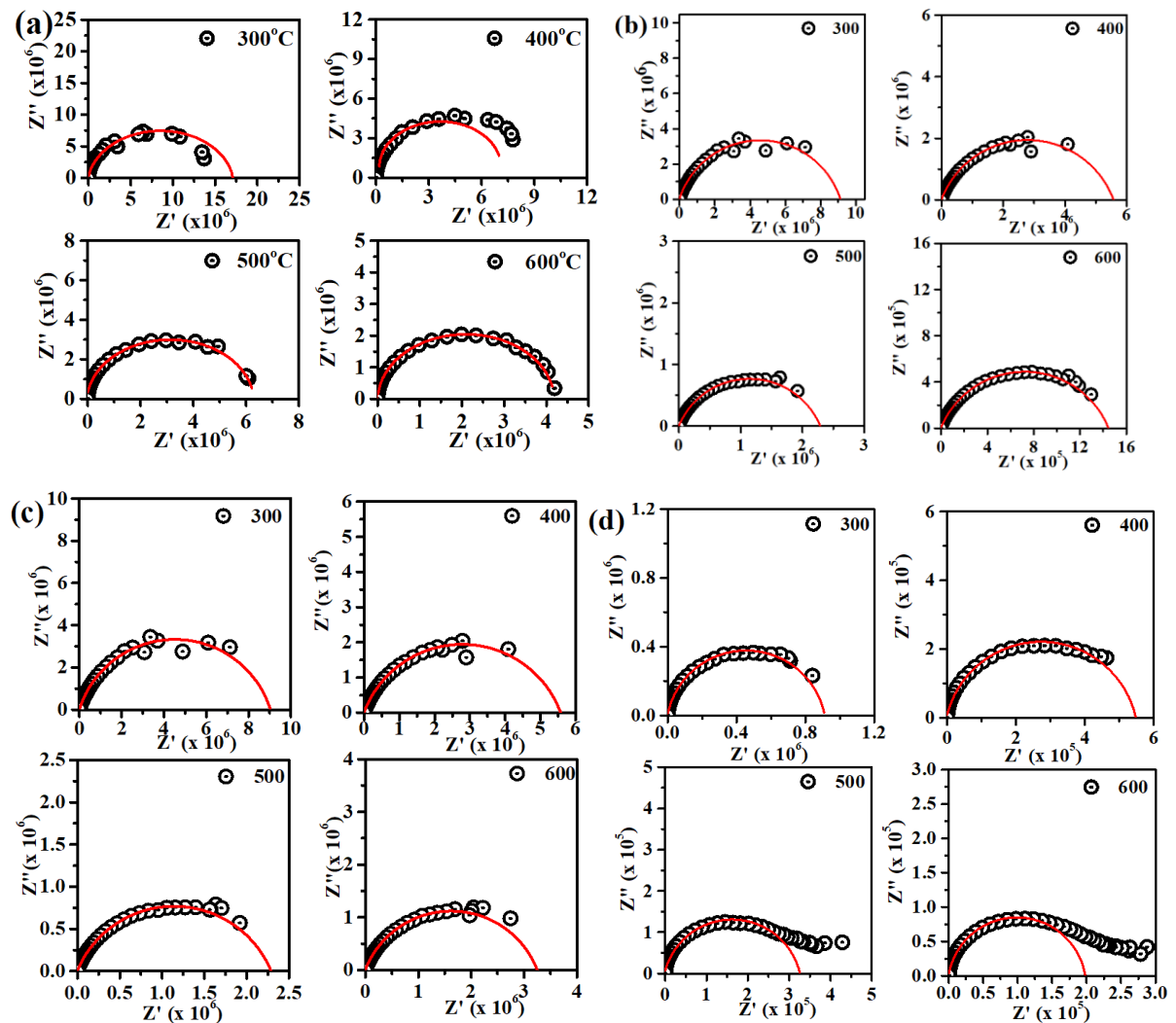


Fig. 14: Nyquist Plot obtained for all samples (a) B2LS0, (b) B2LS1, (c) B2LS2, (d) B2LS4, symbols represent the experimental data point, and solid line shows fitting using equation (16). The illustration of logarithmic of resistance derived from the cole-cole fitting with respect to inverse of temperature was shown in Fig. 15. The activation energy required for the migration of charge carrier within the sample through grain/grain boundary/electrode has been calculated by employing fitting of Arrhenius equation to the experimental data and given in the inset of each fig. The value of activation energy obtained for grain in present case assigned to the migration of electrons between the degenerate sites of Sn^{4+} and Sn^{2+} . Since the order of capacitance reflects the contribution of interface, that might be due to presence of multivalent ion at the interface such as Sn^{4+} . The multivalent ion captures the electron present at the interface and reduced the multivalent states of Sn^{4+} to Sn^{2+} . Since the grain boundary shows higher insulating than grain so that it needs slightly higher activation energy for the migration

of charge carrier [15,59]. With increasing the doping concentration, the value of activation energy found to be gradual increase that might be due to large size of polaron (See Table 3).

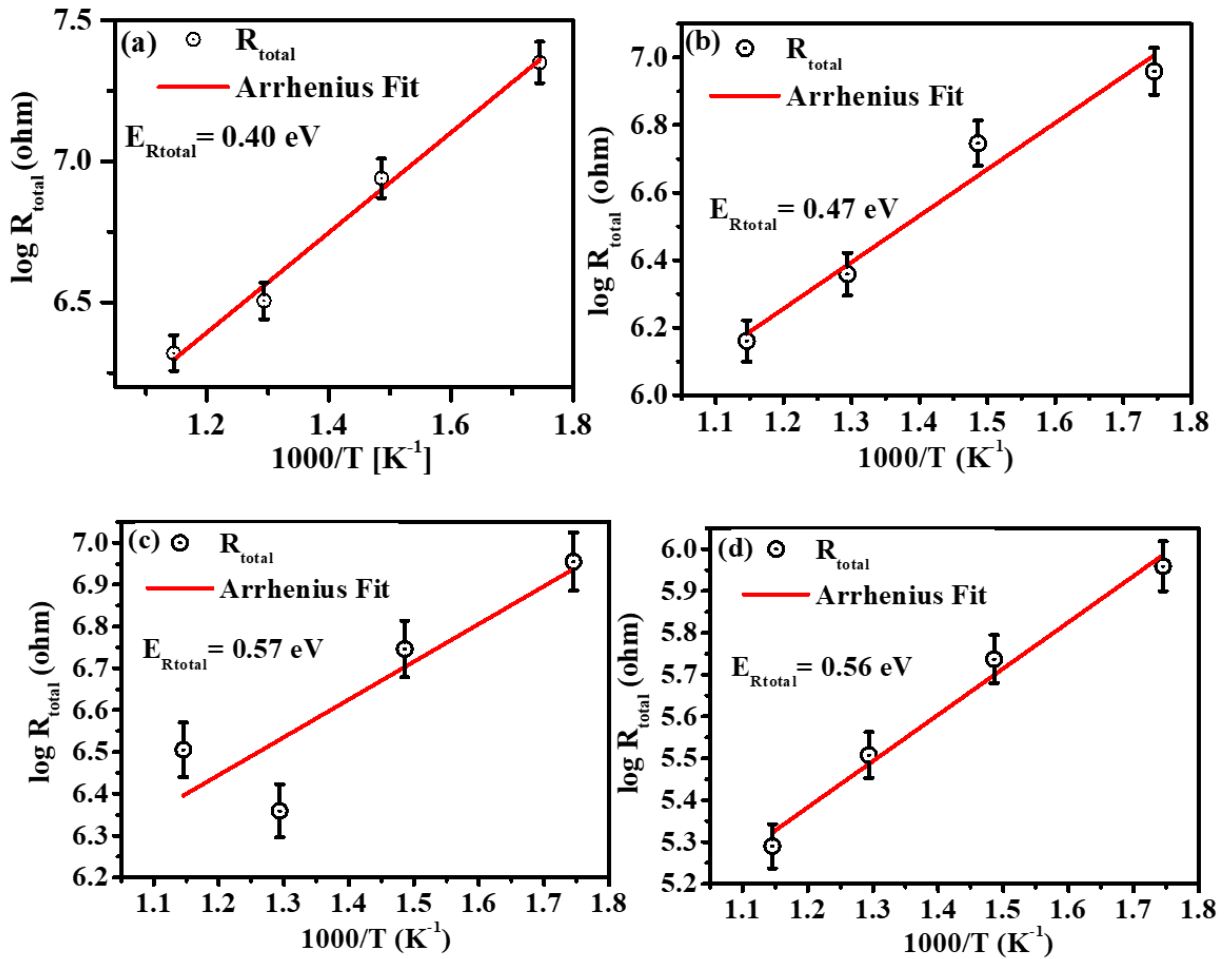


Fig. 15: Variation between the logarithmic of total resistance (R_{total}) with inverse of temperature for all samples, (a) B2LS0 (b) B2LS1 (c) B2LS2 (d) B2LS4

Based on the value of activation energy, the present materials can be utilized as mixed ionic and electronic conductor and semiconductor device applications.

Conclusions:

A few compositions of the system $\text{Ba}_{2-x}\text{La}_x\text{SnO}_4$ (where $x=0, 0.01, 0.02, 0.04, 0.06, 0.10$) have been successfully synthesized using the solid-state ceramic route. The XRD studies along with FTIR, Raman and UV-Vis. study suggests the solubility of La at the site of Ba in Ba_2SnO_4 was limited between 4 to 6 atoms %. The compositions having a doping concentration above than 4 atom % contains impurity of $\text{La}_2\text{Sn}_2\text{O}_7$ pyrochlore phase. Rietveld refinement studies performed on XRD data indicated lower unit cell volume, density, and bond length Ba/La-O1 and Ba/La-O2. The incorporation of La results decrease of crystallite size, and average grain

size whereas increase of micro-strain due to lower ionic radii of La^{3+} than Ba^{2+} . The optical band gap of all samples obtained using Tauc plot was found to be in the range of (3.23-3.75) eV that indicates semiconducting nature of sample. The ac conductivity spectra of all samples follow universal Johnscher's power law. The value of σ_{dc} and f_h derived using Johnscher's power law indicating the presence of Arrhenius type conduction in samples. Two regions of conduction found within the investigated temperature region. The values of activation energy obtained from σ_{dc} and f_h was found almost same that indicates the similar sources are responsible for dc and ac conduction. The ac conduction occurs within the sample via the formation of large polaron overlapping between the neighbouring site that also support from the bond length Ba/La-O1, Ba/La-O2, Sn-O1, Sn-O2 and R_ω derived from OLPT model fitting. Also, the scaled conductivity with respect to scaled frequency nicely superimposed on each other, suggesting that the source of charge carrier found to be same at all temperatures. The major contribution of grain was observed from Nyquist plot further suggesting that the conduction takes place via the overlapping of large polaron tunnelling. Based on the studies, the present materials could be utilized as semiconductor and mixed ionic and electronic conductor (MIECs) in fuel cell application.

Acknowledgement:

The authors are grateful to the Head Department of Physics, Head Department of Pharmaceutics, Head Department of Metallurgical Engineering and Coordinator, Central Instrument Facility Centre (CIFC), IIT(BHU), Varanasi for providing the experimental facilities required for the characterization of the synthesized samples.

Conflict of Interest

There is no any conflict of interest in this manuscript.

Data availability statement

The raw/processed data required to reproduce these findings cannot be shared at this time as the data also a part of an ongoing study.

References:

- [1] D. Lee, H. Lee, Controlling Oxygen Mobility in Ruddlesden–Popper Oxides, *Materials* (Basel). 10 (2017) 368. <https://doi.org/10.3390/ma10040368>.
- [2] C. Navas, H.C. Zur Loye, Conductivity studies on oxygen-deficient Ruddlesden-

- Popper phases, *Solid State Ionics*. 93 (1996) 171–176. [https://doi.org/10.1016/S0167-2738\(96\)00515-2](https://doi.org/10.1016/S0167-2738(96)00515-2).
- [3] P. V. Balachandran, D. Puggioni, J.M. Rondinelli, Crystal-Chemistry Guidelines for Noncentrosymmetric A_2BO_4 Ruddlesden–Popper Oxides, *Inorg. Chem.* 53 (2014) 336–348. <https://doi.org/10.1021/ic402283c>.
- [4] T.L. Meyer, R. Jacobs, D. Lee, L. Jiang, J.W. Freeland, C. Sohn, T. Egami, D. Morgan, H.N. Lee, Strain control of oxygen kinetics in the Ruddlesden-Popper oxide $La_{1.85}Sr_{0.15}CuO_4$, *Nat. Commun.* 9 (2018) 92. <https://doi.org/10.1038/s41467-017-02568-z>.
- [5] M. Wei, W. Che, H. Li, Z. Wang, F. Yan, Y. Liu, J. Liu, Ruddlesden-Popper type $La_2NiO_{4+\delta}$ oxide coated by Ag nanoparticles as an outstanding anion intercalation cathode for hybrid supercapacitors, *Appl. Surf. Sci.* 484 (2019) 551–559. <https://doi.org/10.1016/j.apsusc.2019.04.015>.
- [6] H. Weng, Y. Kawazoe, X. Wan, J. Dong, Electronic structure and optical properties of layered perovskites Sr_2MO_4 ($M=Ti, V, Cr, Mn, \text{ and } Co$): An ab initio study, *Phys. Rev. B - Condens. Matter Mater. Phys.* 74 (2006) 1–9. <https://doi.org/10.1103/PhysRevB.74.205112>.
- [7] U. Kumar, S. Upadhyay, Sr_2SnO_4 Ruddlesden Popper Oxide: Future Material for Renewable Energy Applications, in: *Green Energy*, Wiley, 2020: pp. 221–250. <https://doi.org/10.1002/9781119760801.ch8>.
- [8] K.H. Lee, Y.F. Wang, S.W. Kim, H. Ohta, K. Koumoto, Thermoelectric Properties of Ruddlesden-Popper Phase n-Type Semiconducting Oxides: La-, Nd-, and Nb-Doped $Sr_3Ti_2O_7$, *Int. J. Appl. Ceram. Technol.* 4 (2007) 326–331. <https://doi.org/10.1111/j.1744-7402.2007.02147.x>.
- [9] R. Zhang, M.S. Senn, M.A. Hayward, Directed Lifting of Inversion Symmetry in Ruddlesden–Popper Oxide–Fluorides: Toward Ferroelectric and Multiferroic Behavior, *Chem. Mater.* 28 (2016) 8399–8406. <https://doi.org/10.1021/acs.chemmater.6b03931>.
- [10] L. Miao, J. Hou, Z. Gong, Z. Jin, W. Liu, A high-performance cobalt-free Ruddlesden-Popper phase cathode $La_{1.2}Sr_{0.8}Ni_{0.6}Fe_{0.4}O_{4+\delta}$ for low temperature proton-conducting solid oxide fuel cells, *Int. J. Hydrogen Energy*. 44 (2019) 7531–7537. <https://doi.org/10.1016/j.ijhydene.2019.01.255>.
- [11] G. Amow, S.J. Skinner, Recent developments in Ruddlesden–Popper nickelate systems for solid oxide fuel cell cathodes, *J. Solid State Electrochem.* 10 (2006) 538–546.

- <https://doi.org/10.1007/s10008-006-0127-x>.
- [12] A. Jun, T. Lim, J. Shin, G. Kim, Electrochemical properties of B-site Ni doped layered perovskite cathodes for IT-SOFCs, *Int. J. Hydrogen Energy*. 39 (2014) 20791–20798. <https://doi.org/10.1016/j.ijhydene.2014.06.136>.
- [13] A. Manthiram, J.-H. Kim, Y.N. Kim, K.-T. Lee, Crystal chemistry and properties of mixed ionic-electronic conductors, *J. Electroceramics*. 27 (2011) 93–107. <https://doi.org/10.1007/s10832-011-9635-x>.
- [14] K.S. Yun, J.H. Park, Y. Kwon, D.Y. Kim, C.-Y. Yoo, J.H. Yu, J.H. Joo, A new strategy for enhancing the thermo-mechanical and chemical stability of dual-phase mixed ionic electronic conductor oxygen membranes, *J. Mater. Chem. A*. 4 (2016) 13549–13554. <https://doi.org/10.1039/C6TA04361E>.
- [15] U. Kumar, S. Upadhyay, Structural, Optical and Electrical Properties of Ruddlesden Popper Oxide Ba₂SnO₄, *J. Electron. Mater.* 48 (2019) 5279–5293. <https://doi.org/10.1007/s11664-019-07336-x>.
- [16] A.P. Khandale, J.D. Punde, S.S. Bhoga, Electrochemical performance of strontium-doped neodymium nickelate mixed ionic–electronic conductor for intermediate temperature solid oxide fuel cells, *J. Solid State Electrochem.* 17 (2013) 617–626. <https://doi.org/10.1007/s10008-012-1892-3>.
- [17] C. Jin, J. Liu, Y. Zhang, J. Sui, W. Guo, Characterization and electrochemical performances of Ba_{2-x}Sr_xFeO_{4+δ} as a novel cathode material for intermediate-temperature solid oxide fuel cells, *J. Power Sources*. 182 (2008) 482–488. <https://doi.org/10.1016/j.jpowsour.2008.04.044>.
- [18] S. Science, Sol–gel (combustion) synthesis and characterization of different alkaline earth metal (Ca, Sr, Ba) stannates, *J. Sol-Gel Sci. Technol.* 64 (2012) 643–652. <https://doi.org/10.1007/s10971-012-2896-2>.
- [19] A. Kareiva, S. Šakirzanovas, T. Jüstel, M. Van Bael, A. Katelnikovas, D. Dutczak, D. Enseling, A. Stanulis, A. Hardy, Luminescence properties of Sm³⁺-doped alkaline earth ortho-stannates, *Opt. Mater. (Amst)*. 36 (2014) 1146–1152. <https://doi.org/10.1016/j.optmat.2014.02.018>.
- [20] H. Gao, Y. Wang, Photoluminescence of Eu³⁺ activated Ba₂SnO₄ under ultraviolet-vacuum ultraviolet excitation, *J. Mater. Res.* 21 (2006) 1857–1861. <https://doi.org/10.1557/jmr.2006.0230>.
- [21] J. Zhang, R. Hu, Q. Qin, D. Wang, B. Liu, Y. Wen, M. Zhou, Y. Wang, The origin of two quenching concentrations and unusual afterglow behaviors of Ba₂SnO₄:Sm³⁺

- phosphor, *J. Lumin.* 132 (2012) 2590–2594.
<https://doi.org/10.1016/j.jlumin.2012.05.027>.
- [22] U. Kumar, K. Ankur, D. Yadav, S. Upadhyay, Synthesis and characterization of Ruddlesden-Popper system ($\text{Ba}_{1-x}\text{Sr}_x$) $_2\text{SnO}_4$, *Mater. Charact.* 162 (2020) 110198.
<https://doi.org/10.1016/j.matchar.2020.110198>.
- [23] M. Yasukawa, T. Kono, K. Ueda, H. Yanagi, H. Hosono, High-temperature thermoelectric properties of La-doped BaSnO_3 ceramics, *Mater. Sci. Eng. B.* 173 (2010) 29–32.
- [24] B.C. Luo, J. Zhang, J. Wang, P.X. Ran, Structural, electrical and optical properties of lanthanum-doped barium stannate, *Ceram. Int.* 41 (2015) 2668–2672.
- [25] C. Shan, T. Huang, J. Zhang, M. Han, Y. Li, Z. Hu, J. Chu, Optical and Electrical Properties of Sol–Gel Derived $\text{Ba}_{1-x}\text{La}_x\text{SnO}_3$ Transparent Conducting Films for Potential Optoelectronic Applications, *J. Phys. Chem. C.* 118 (2014) 6994–7001.
- [26] U.S. Alaan, F.J. Wong, J.J. Ditto, A.W. Robertson, E. Lindgren, A. Prakash, G. Haugstad, P. Shafer, D. Johnson, E. Arenholz, Magnetism and transport in transparent high-mobility BaSnO_3 films doped with La, Pr, Nd, and Gd, *Phys. Rev. Mater.* 3 (2019) 124402.
- [27] K.K. James, P.S. Krishnaprasad, K. Hasna, M.K. Jayaraj, Structural and optical properties of La-doped BaSnO_3 thin films grown by PLD, *J. Phys. Chem. Solids.* 76 (2015) 64–69. <https://doi.org/10.1016/j.jpics.2014.07.024>.
- [28] Q. Liu, J. Liu, B. Li, H. Li, G. Zhu, K. Dai, Z. Liu, P. Zhang, J. Dai, Composition dependent metal-semiconductor transition in transparent and conductive La-doped BaSnO_3 epitaxial films, *Appl. Phys. Lett.* 101 (2012) 241901.
- [29] M.J. Ansaree, S. Upadhyay, Electrical characterization of porous La-doped BaSnO_3 using impedance spectroscopy, *Ionics (Kiel)*. 21 (2015) 2825–2838.
<https://doi.org/10.1007/s11581-015-1476-1>.
- [30] M. Yasukawa, T. Kono, K. Ueda, H. Yanagi, H. Hosono, High-temperature thermoelectric properties of La-doped BaSnO_3 ceramics, *Mater. Sci. Eng. B Solid-State Mater. Adv. Technol.* 173 (2010) 29–32.
<https://doi.org/10.1016/j.mseb.2009.10.002>.
- [31] S. Upadhyay, O. Parkash, D. Kumar, Solubility of lanthanum, nickel and chromium in barium stannate, *Mater. Lett.* 49 (2001) 251–255. [https://doi.org/10.1016/S0167-577X\(00\)00378-5](https://doi.org/10.1016/S0167-577X(00)00378-5).
- [32] U. Kumar, D. Yadav, S. Upadhyay, Investigation of structural, optical, and magnetic

- properties of Nd-doped Sr₂SnO₄ Ruddlesden Popper oxide, *J. Am. Ceram. Soc.* 103 (2020) 5743–5757. <https://doi.org/10.1111/jace.17303>.
- [33] U. Kumar, S. Upadhyay, Structural, microstructure, optical, and dielectric properties of Sr_{1.99}M_{0.01}SnO₄ (M: La, Nd, Eu) Ruddlesden–Popper oxide, *J. Mater. Sci. Mater. Electron.* 31 (2020) 5721–5730. <https://doi.org/10.1007/s10854-020-03140-0>.
- [34] B.J. Kennedy, Neutron powder diffraction study of Sr₂SnO₄ and Ba₂SnO₄, *Aust. J. Chem.* 50 (1997) 917–920. <https://doi.org/10.1071/C971117>.
- [35] T. Truttmann, A. Prakash, J. Yue, T.E. Mates, B. Jalan, Dopant solubility and charge compensation in La-doped SrSnO₃ films, *Appl. Phys. Lett.* 115 (2019) 152103. <https://doi.org/10.1063/1.5119272>.
- [36] U. Kumar, D. Yadav, A.K. Thakur, K.K. Srivastav, S. Upadhyay, Investigation on phase formation of Sr₂SnO₄ and effect of La-doping on its structural and optical properties, *J. Therm. Anal. Calorim.* 135 (2019) 1987–1999. <https://doi.org/10.1007/s10973-018-7432-3>.
- [37] L. Ai, Z. Wang, C. Cui, W. Liu, L. Wang, Catalytic Oxidation of Soot on a Novel Active Ca-Co Dually-Doped Lanthanum Tin Pyrochlore Oxide, *Materials (Basel)*. 11 (2018) 653. <https://doi.org/10.3390/ma11050653>.
- [38] U. Venkateswaran, K. Strössner, K. Syassen, G. Burns, M.W. Shafer, Pressure dependence of the Raman modes in Sr₂TiO₄, *Solid State Commun.* 64 (1987) 1273–1277. [https://doi.org/10.1016/0038-1098\(87\)90624-7](https://doi.org/10.1016/0038-1098(87)90624-7).
- [39] A. Kumar, B. Khan, G. Singh, A. Dixit, U. Kumar, M.K. Singh, Structural, microstructure, optical, and electrical properties of Ti-doped CaSnO₃ prepared by Sol-Gel chemical route, *Phys. Scr.* 95 (2020) 105807. <https://doi.org/10.1088/1402-4896/abb89f>.
- [40] U. Kumar, S. Upadhyay, P.A. Alvi, Study of reaction mechanism, structural, optical and oxygen vacancy-controlled luminescence properties of Eu-modified Sr₂SnO₄ Ruddlesden popper oxide, *Phys. B Condens. Matter.* 604 (2021) 412708. <https://doi.org/10.1016/j.physb.2020.412708>.
- [41] U. Kumar, J. Ansaree, S. Upadhyay, Structural and optical characterizations of BaSnO₃ nanopowder synthesized by aqueous sol-gel method, *Process. Appl. Ceram.* 11 (2017) 177–184.
- [42] S. Omeiri, N. Allalou, G. Rekhila, Y. Bessekhoud, M. Trari, Preparation and characterization of nano structured Ba₂SnO₄ as a novel photocatalyst material for the chromate reduction, *Appl. Nanosci.* 4 (2014) 959–966. <https://doi.org/10.1007/s13204->

013-0276-z.

- [43] T. Yamashita, K. Ueda, Blue photoluminescence in Ti-doped alkaline-earth stannates, *J. Solid State Chem.* 180 (2007) 1410–1413.
<https://doi.org/10.1016/j.jssc.2007.02.009>.
- [44] H. Cheema, S. Kumar, P.A. Alvi, B.L. Choudhary, U. Kumar, Synthesis and physical properties of nanopowder and electrical properties of bulk samples of $\text{ZnFe}_{2-x}\text{Ni}_x\text{O}_4$ (x : 0, 0.05, 0.10), *Adv. Powder Technol.* 31 (2020) 4241–4252.
<https://doi.org/10.1016/j.appt.2020.09.001>.
- [45] H. JAFFE, Piezoelectric Ceramics, *J. Am. Ceram. Soc.* 41 (1958) 494–498.
<https://doi.org/10.1111/j.1151-2916.1958.tb12903.x>.
- [46] U. Kumar, M.J. Ansaree, A.K. Verma, S. Upadhyay, G. Gupta, Oxygen vacancy induced electrical conduction and room temperature ferromagnetism in system $\text{BaSn}_{1-x}\text{Ni}_x\text{O}_3$ ($0 < x < 0.20$), *Mater. Res. Express.* 4 (2017) 116304.
<https://doi.org/10.1088/2053-1591/aa9416>.
- [47] R.D. Shannon, C.T. Prewitt, Revised values of effective ionic radii, *Acta Crystallogr. Sect. B Struct. Crystallogr. Cryst. Chem.* 26 (1970) 1046–1048.
<https://doi.org/10.1107/S0567740870003576>.
- [48] A. Kumar, B. Khan, V. Yadav, A. Dixit, U. Kumar, M.K. Singh, Rietveld refinement, optical, dielectric and ac conductivity studies of Ba-doped SrSnO_3 , *J. Mater. Sci. Mater. Electron.* 31 (2020) 16838–16848. <https://doi.org/10.1007/s10854-020-04240-7>.
- [49] X. Yang, S. Liu, F. Lu, J. Xu, X. Kuang, Acceptor Doping and Oxygen Vacancy Migration in Layered Perovskite NdBaInO_4 -Based Mixed Conductors, *J. Phys. Chem. C.* 120 (2016) 6416–6426. <https://doi.org/10.1021/acs.jpcc.6b00700>.
- [50] S. Kabi, A. Ghosh, Ion dynamics in glassy ionic conductors: Scaling of mean square displacement of mobile ions, *EPL (Europhysics Lett.)* 108 (2014) 36002.
<https://doi.org/10.1209/0295-5075/108/36002>.
- [51] N. Chakchouk, B. Louati, K. Guidara, Electrical properties and conduction mechanism study by OLPT model of NaZnPO_4 compound, *Mater. Res. Bull.* 99 (2018) 52–60.
<https://doi.org/10.1016/j.materresbull.2017.10.046>.
- [52] A. Zaafouri, M. Megdiche, M. Gargouri, Studies of electric, dielectric, and conduction mechanism by OLPT model of $\text{Li}_4\text{P}_2\text{O}_7$, *Ionics (Kiel)*. 21 (2015) 1867–1879.
<https://doi.org/10.1007/s11581-015-1365-7>.
- [53] S. Nasri, M. Megdiche, M. Gargouri, DC conductivity and study of AC electrical

- conduction mechanisms by non-overlapping small polaron tunneling model in LiFeP₂O₇ ceramic, *Ceram. Int.* 42 (2016) 943–951.
<https://doi.org/10.1016/j.ceramint.2015.09.023>.
- [54] S. Singh, P.A. Jha, S. Varma, P. Singh, Large polaron hopping phenomenon in lanthanum doped strontium titanate, *J. Alloys Compd.* 704 (2017) 707–716.
<https://doi.org/10.1016/j.jallcom.2017.02.015>.
- [55] R. Kurre, S. Bajpai, P.K. Bajpai, Synthesis, characterization, optical and transport properties of BaSnO₃ synthesized by wet chemical route, *Mater. Sci. Appl.* 9 (2018) 92.
- [56] S. Murugavel, M. Upadhyay, AC conduction in amorphous semiconductors, *J. Indian Inst. Sci.* 91 (2011) 303–318.
- [57] J.R. Macdonald, W.B. Johnson, Fundamentals of Impedance Spectroscopy, in: *Impedance Spectrosc. Theory, Exp. Appl. Second Ed.*, 2005.
<https://doi.org/10.1002/0471716243.ch1>.
- [58] S.K. Kim, M. Miyayama, H. Yanagida, Complex impedance and modulus analysis on electrical anisotropy of layer-structured BaBi₄Ti₄O₁₅ single crystal in paraelectric phase, *Nippon Seramikkusu Kyokai Gakujutsu Ronbunshi/Journal Ceram. Soc. Japan.* (1995). <https://doi.org/10.2109/jcersj.103.315>.
- [59] U. Kumar, S. Upadhyay, Studies on dielectric and electrical properties of Ruddlesden-Popper oxide Sr₂SnO₄, *Mater. Lett.* 227 (2018) 100–103.
<https://doi.org/10.1016/j.matlet.2018.05.046>.